Geological Magazine

www.cambridge.org/geo

New granular rock-analogue materials for simulation of multi-scale fault and fracture processes

L. Massaro[1], J. Adam[1], E. Jonade[1] and Y. Yamada[1,2]

[1]Department of Earth Sciences, Royal Holloway University of London, Egham, United Kingdom and [2]Department of Earth Resources Engineering, Kyushu University, Fukuoka, Japan

Original Article

Cite this article: Massaro L, Adam J, Jonade E, and Yamada Y (2023) New granular rock-analogue materials for simulation of multi-scale fault and fracture processes. *Geological Magazine* **159**: 2036–2059. https://doi.org/10.1017/S0016756821001321

Received: 2 June 2021
Revised: 22 November 2021
Accepted: 23 November 2021
First published online: 27 December 2021

Keywords:
Analogue modelling; granular materials; scaling; rock mechanics; fault damage zone

Author for correspondence:
L. Massaro,
Email: Luigi.Massaro.2018@live.rhul.ac.uk

Abstract

In this study, we present a new granular rock-analogue material (GRAM) with a dynamic scaling suitable for the simulation of fault and fracture processes in analogue experiments. Dynamically scaled experiments allow the direct comparison of geometrical, kinematical and mechanical processes between model and nature. The geometrical scaling factor defines the model resolution, which depends on the density and cohesive strength ratios of model material and natural rocks. Granular materials such as quartz sands are ideal for the simulation of upper crustal deformation processes as a result of similar nonlinear deformation behaviour of granular flow and brittle rock deformation. We compared the geometrical scaling factor of common analogue materials applied in tectonic models, and identified a gap in model resolution corresponding to the outcrop and structural scale (1–100 m). The proposed GRAM is composed of quartz sand and hemihydrate powder and is suitable to form cohesive aggregates capable of deforming by tensile and shear failure under variable stress conditions. Based on dynamical shear tests, GRAM is characterized by a similar stress–strain curve as dry quartz sand, has a cohesive strength of 7.88 kPa and an average density of 1.36 g cm^{-3}. The derived geometrical scaling factor is 1 cm in model = 10.65 m in nature. For a large-scale test, GRAM material was applied in strike-slip analogue experiments. Early results demonstrate the potential of GRAM to simulate fault and fracture processes, and their interaction in fault zones and damage zones during different stages of fault evolution in dynamically scaled analogue experiments.

1. Introduction

Natural faults and fractures form the most common geological structures and control the mechanical strength and fluid flow in the Earth's crust. These structures exist on all scales, ranging from regional fault systems and individual faults to fracture systems and micro-cracks in fault damage zones. Faults are complex four-dimensional (4D) structures consisting of heterogeneously deformed volumes of country rock, and characterized by a complex spatial and temporal evolution of their structural and fluid flow properties. Fault and fractures show typical self-similar or scale-invariant characteristics and are characterized by highly variable strains and transient nonlinear deformation mechanisms. Structural and petrophysical analyses therefore strongly depend on the observational scale, ranging from regional to micro-scales. The smaller the scale, the smaller the faults that are observable (Wibberley & Shipton, 2010).

Fault zones are composed of rocks in variable degrees of deformation, consisting of a high-strain fault core with one or several slip zones, gouge and breccias embedded in a low-strain fracture-dominated 'damage zone' (Billi *et al.* 2003; Kim *et al.* 2004; Choi *et al.* 2016). Strain localization leads to the progressive abandonment of many distributed small faults in the stress shadow of a few larger faults, which then accumulate further displacement. Due to the spatial and temporal heterogeneity of faults and fault zones, the investigation of fault and fracture processes critically depends on the range of spatial and temporal observation scales (Fig. 1).

The comprehension of a fault system and the related fracture network architectures has a critical societal impact involving many areas of geosciences, including the development of important predictive tools and modelling techniques, from the exploration and management of natural resources to the analysis and mitigation of environmental hazards.

Despite extensive geological field studies and laboratory-based material tests, the analysis of these multi-scale deformation processes in fault zones and the identification of their underlying fundamental processes remain a challenge. Rock mechanic tests of brittle rocks have confirmed the complex rheology and contrasting nonlinear deformation mechanisms that are controlled by variable stress conditions in the Earth's crust. However, laboratory rock mechanics results cannot be scaled up easily to large fault–fracture systems. Mechanical fault models and numerical continuum finite-element (FE) modelling techniques apply only simplified mathematical

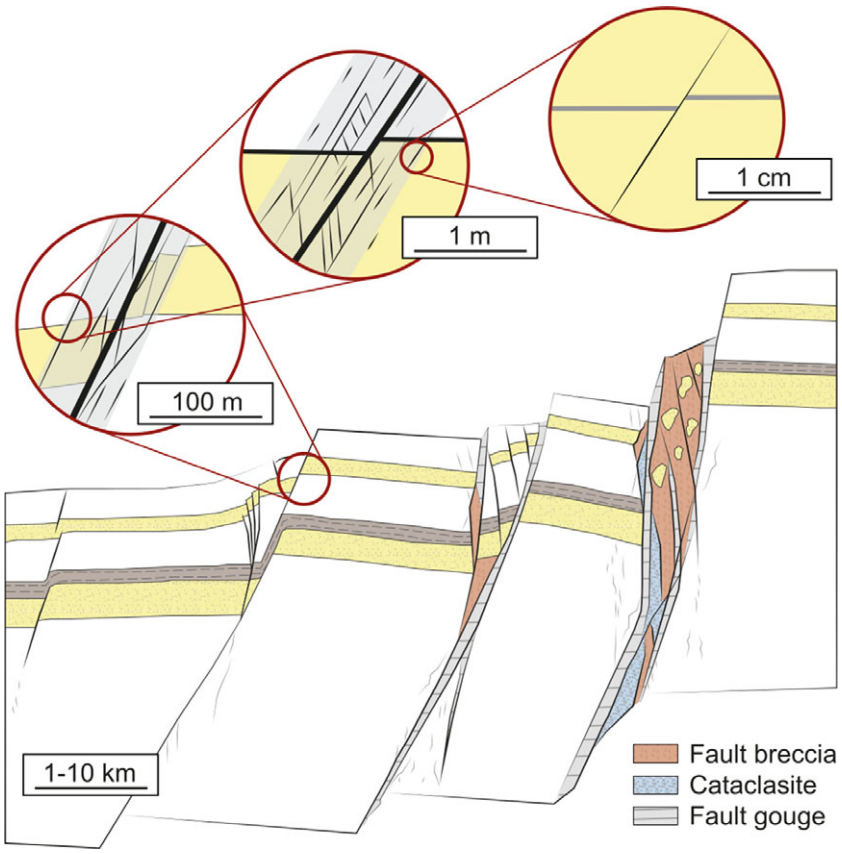

Fig. 1. Complexity of fault systems shown in terms of observation scale and strain evolution (modified after Wibberley & Shipton, 2010; Fossen, 2020).

models of the relevant physical processes (e.g. Coulomb rheology), and do not achieve the required spatial resolution for simulating complex multi-scale fault–fracture systems (Davis, 1984; Mandl, 1988; Twiss & Moores, 1992).

Analogue modelling techniques provide an important tool for the spatial and temporal investigation of tectonic processes. For the simulation of upper crustal deformation processes, cohesion-less granular materials, such as dry quartz sand, are widely used (Reber *et al.* 2020). These materials show nonlinear frictional properties similar to natural rocks and are ideal to simulate the 3D architecture of complex regional-scale fault systems. On the other hand, cohesion-less granular materials are not able to form extension fractures and cannot provide suitable dynamic scaling and spatial resolution for the simulation of fault–fracture networks in fault damage zones.

In this study, we present a new granular rock-analogue material (GRAM; introduced by Chemenda *et al.* 2011) with scaled physical and mechanical parameters for the realistic simulation of multi-scale fault–fracture processes in scaled physical experiments. GRAM development was based on quartz sand aggregates prepared with the addition of different materials acting as cementing agents, such as gelatine, sugar, vegetable oil and hemihydrate powder. The mechanical properties of the four potential aggregates were qualitative and quantitatively tested by means of ring-shear tests (RSTs) and uniaxial compression tests (UCTs).

Sand–hemihydrate samples appeared to be the most suitable GRAM candidate, capable of deforming by shear and tensile failure under variable loading conditions, while maintaining the nonlinear elastic-frictional-plastic properties of granular solids such as dry sand. The dynamic scaling provided by this model material enabled the simulation at the targeted model resolution, with 1 cm in the model corresponding to the outcrop scale (1–100 m). Furthermore, the mechanical properties of the key material can be adjusted by applying different mixing ratios of sand and hemihydrate, allowing adjustment of the model resolution and geometrical scaling.

As a proof-of-concept, we tested GRAM for the simulation of fault initiation and localization in a low-strain strike-slip damage zone by performing a series of strike-slip experiments, monitored and analysed by digital image correlation (DIC) techniques. The experiment series confirmed the suitability of the sand–hemihydrate GRAM material for the simulation of coupled fault–fracture processes in dynamically scaled analogue experiments. Mechanical analysis of integrated fault–fracture processes observed in GRAM experiments will provide an improved understanding of the formation, growth and co-evolution of fault–fracture systems in the subsurface. The simulation of coupled fault–fracture processes in scaled analogue experiments can help to develop predictive tools for the understanding of such complex structures, analysing the dynamical interaction of faults and fractures during the different stages of deformation.

2. Geological background

2.a. Faults and fractures

Failure occurs in a material when it is unable to support the acting stress state without permanent deformation. Brittle failure is represented by a surface where the material loses cohesion and breaks apart, whereas in ductile failure the permanent deformation occurs without losing cohesion. In the brittle field, two main types of fractures are identified as end-members of the deformation process,

https://doi.org/10.1017/S0016756821001321 Published online by Cambridge University Press

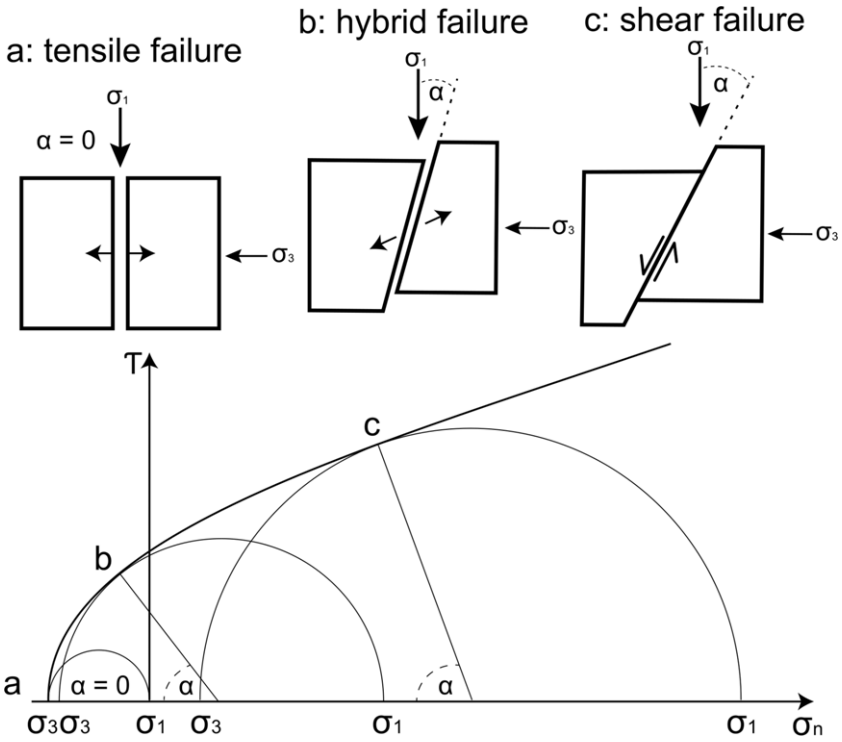

Fig. 2. Graphic representation of the combined criteria defining tensile, hybrid and shear failure.

namely shear and tensile failure. Their occurrence depends on several conditions, including the acting stress field and differential stresses. The state of stress at a point can be graphically represented by Mohr diagrams (Fig. 2) where the failure envelope, defined by the Mohr circles, represents the critical stresses at failure on a set of planes (Twiss & Moores, 1992). The normal and shear stresses acting on all existing and potential planes change systematically with the orientation of the plane (Hoek & Brown, 1988).

Depending on the stress conditions in the upper crust, rocks exhibit a wide range of rheologies (Hoek & Martin, 2014). At the regional scale, faults can be classified with respect to the principal stress tensor orientation (Anderson, 1951), and a simplified Coulomb rheology can be applied for fault mechanics analysis (Davis, 1984; Mandl, 1988; Twiss & Moores, 1992).

At a smaller scale, as demonstrated by rock mechanics laboratory tests, when subjected to large differential stresses, rocks show a nonlinear strain-dependent elastic/frictional behaviour with contrasting deformation mechanisms under variable stress conditions. The contrasting deformation processes include elastic deformation, plastic deformation with strain softening and strain hardening, strain-dependent strength, transient deformation mechanisms, frictional sliding, cataclastic flow and tensile, compressional or shear failure (Byerlee, 1978; Paterson, 1978; Mandl, 1988; Krantz, 1991; Schellart, 2000; Marcher & Vermeer, 2001; Lohrmann *et al.* 2003; Panien *et al.* 2006). On the other hand, when undergoing small differential stresses rocks deform by tensile failure with the formation of cracks, tension gashes or extension fractures (Hoek & Bieniawski, 1965; Basu *et al.* 2013).

Across different scales of observations, the initiation of faults in brittle rocks is controlled by tensile cracks and extension fracturing, growing by coalescence of pre-existing sub-parallel tensile structures, represented by joints, veins or pressure solution seams (Reches & Lockner, 1994; Moore & Lockner, 1995; Peacock & Sanderson, 1995; Scholz, 2002; Healy *et al.* 2006; Choi *et al.* 2016). Their geometries and stress interactions during fault growth influence the fault evolution and orientation (Healy *et al.* 2006; Scholz, 2002). Mode I tensile fracturing therefore occurs first, then the structures link together in a locally perturbed stress field and, eventually, a through-going slip surface develops, allowing modes II and III shear fracturing to occur as a secondary fracture mechanism (Crider & Peacock, 2004).

2.b. Fault zones

A fault system is a complex volume of deformed rock, within which differently strained zones, and related structures, are observed (Wibberley *et al.* 2008; Faulkner *et al.* 2010). These are classified as internal fault zone and enveloping damage zones (Chester & Logan, 1987; Caine *et al.* 1996; Childs *et al.* 1996; Vermilye & Scholz, 1998; Wibberley *et al.* 2008; Faulkner *et al.* 2010). The central fault core accommodates most of the displacement (Micarelli *et al.* 2006; Ferrill *et al.* 2011), is relatively highly strained and, depending on the type of rocks involved, consists of unconsolidated clay-rich gouge zones, breccia, cataclasite and ultracataclasite. The surrounding damage zone shows, at different scales, lower-strain deformation structures such as microfractures, outcrop-scale fracture networks, veins, cleavage, folds and deformation bands, enhancing the fault zone permeability. Strictly depending on the observation scale, several faults of different orders are contained within this fault volume (Billi *et al.* 2003; Kim *et al.* 2004; Faulkner *et al.* 2010; Choi *et al.* 2016).

The damage zone is, in turn, surrounded by the undeformed host rock, representing a transition between the zones of high-deformation and non-deformation. The fault damage zone is closely associated with the fundamental processes of fault initiation, growth, termination and long-term evolution (Cowie & Shipton, 1998; Peacock, 2002; Kim *et al.* 2003, 2004; Shipton & Cowie, 2003; Gudmundsson *et al.* 2010). Damage zones are seen in many geological disciplines as the key factor controlling overall fault properties, for example, the regional tectonic evolution (Scholz & Cowie, 1990;

https://doi.org/10.1017/S0016756821001321 Published online by Cambridge University Press

Marrett & Allmendinger, 1992; Walsh *et al.* 1999), earthquake faulting and seismic hazards (Sibson, 1989; Kim & Sanderson, 2009; Choi *et al.* 2012), fluid flow in the Earth crust (Simpson *et al.* 2003; Faulkner *et al.* 2010), groundwater flow (Gudmundsson *et al.* 2013), hydrocarbon and mineral resources (Aydin, 2000) and CO_2 storage (Shipton *et al.* 2004).

2.c. Analogue modelling

Over the last two centuries, analogue models have provided a powerful tool for the investigation of complex deformation processes and their geometric, kinematic and dynamic aspects (McClay & Ellis, 1987*b*; Huiqui *et al.* 1992; Lallemand *et al.* 1994; Schreurs, 1994; Gutscher *et al.* 1996; McClay, 1996; Wang & Davis, 1996; Kukowski *et al.* 2002; Adam *et al.* 2005). This method allows the systematic analysis of the formation and evolution of geological structures in space and time, whereas the natural outcrop represents just a single 'frame' of the entire process. In scaled models, different boundary conditions and parameters can be tested and quantified, enabling the evaluation of their influence on the overall process.

Furthermore, the development of new technologies constantly improves the deformation monitoring of the experiments, by means of high-resolution imaging techniques. These include strain monitoring with particle image velocimetry (Bitri *et al.* 1997; White *et al.* 2001; Adam *et al.* 2002; Wolf *et al.* 2003), digital image correlation (DIC) (Adam *et al.* 2005; Hoth *et al.* 2006, 2007, 2008; Cruz *et al.* 2008, 2010; Pons & Mourgues, 2012; Yamada *et al.* 2014; Dotare *et al.* 2016) and integrated digital volume correlation (DVC) and X-ray computed tomography (XRCT) techniques (Adam *et al.* 2008, 2013*b*; Zwaan *et al.* 2017).

Nevertheless, scaled analogue models present some limitations that need to be considered when comparing the model with the natural system. These limitations are mainly represented by the boundary conditions acting in natural systems, which cannot be represented easily in laboratory-based experiments, such as pore-fluid pressure, compaction of sediments, and thermal, flexural and isostatic effects.

2.c.1. Scaling

To ensure an appropriate comparison between the analogue models and the natural prototype, laboratory experiments require to be properly scaled with respect to the simulated natural rocks. The scaling theory, first developed by (Hubbert, 1937), represented a turning point for analogue modelling, evolving from a qualitative to a quantitative method.

The scaling procedure is composed of three hierarchical levels of similarity, namely geometric, kinematic and dynamic similarity. Geometric scaling is ensured by proportional corresponding lengths and equal corresponding angles between model and prototype; a similar sequence of deformation proportional in time is additionally required for kinematic scaling; and dynamic scaling also involves the similarity of proportional applied forces and stresses in the model and natural prototype.

In detail, the dynamic scaling is mainly defined by density, frictional parameters and cohesive strength of prototype and model material. The latter therefore plays a critical role in the investigation method. The model material must show a similar angle of internal friction with respect to the upper crustal rocks, 27–45° (Handin, 1966; Jaeger & Cook, 1969), and the following equation must be satisfied (Hubbert, 1937; Ramberg, 1981):

$$\frac{C_m}{C_n} = \frac{\rho_m}{\rho_n}\frac{g_m}{g_n}\frac{L_m}{L_n} \quad (1)$$

where C is cohesive strength, ρ is density, g is gravity, L is length and m and n refer to the model and natural prototype, respectively. For experiments run in normal gravity conditions, the ratio $g_m/g_n = 1$ and Equation (1) can be rewritten as:

$$\frac{L_m}{L_n} = \frac{C_m}{C_n}\frac{\rho_n}{\rho_m}. \quad (2)$$

This length equivalence, determined by cohesive strength and the density of the model material and the natural prototype, is referred to as the geometrical scaling factor, and defines the resolution of the model. The choice of the model material therefore controls the dynamic scaling provided and, consequently, the natural processes scale (Fig. 3).

2.c.2. Analogue materials

The physical and mechanical properties of the analogue materials determine the model resolution, and therefore the deformation scales we can simulate and observe in the experiment. The model material must have similar rheology with respect to the examined prototype and mechanical properties, suitable to be scaled into the target observational scale. Handling and preparation of the experiment samples, as well as their homogeneity and reproducibility, also need to be considered as aspects of primary impact on the model results (Lohrmann *et al.* 2003; Schreurs *et al.* 2006, 2016). The wide range of model materials applied to simulate different tectonic processes has been summarized and discussed in different review articles (Koyi, 1997; Ranalli, 2001; Reber *et al.* 2020), classifying them as materials used to model (1) the upper crust, (2) the middle crust, and (3) the lower crust and the mantle. These include sand (Davis & Dahlen, 1983; McClay & Ellis, 1987*a*; Krantz, 1991; McClay, 1996; Gutscher *et al.* 1998; McClay *et al.* 1998; Bonini *et al.* 2000; Schellart, 2000; Cobbold *et al.* 2001; Lohrmann *et al.* 2003; Panien *et al.* 2006; Dooley & Schreurs, 2012; Gomes, 2013; Wu *et al.* 2015; Dotare *et al.* 2016; Klinkmüller *et al.* 2016; Maestrelli *et al.* 2021; Santolaria *et al.* 2021), gelatine (Corbi *et al.* 2013; van Dinther *et al.* 2013; Brizzi *et al.* 2016), foam rubber (Rosenau & Oncken, 2009; Rosenau *et al.* 2009, 2017), clays (Krantz, 1991; Henza *et al.* 2010; Gomes, 2013; Bonini *et al.* 2016; Bonanno *et al.* 2017; Hatem *et al.* 2017), silica powder (Galland *et al.* 2006; Abdelmalak *et al.* 2016), hemihydrate powder (Holland *et al.* 2006; Panien *et al.* 2006; van Gent *et al.* 2010; von Hagke *et al.* 2019; Poppe *et al.* 2021), glass microspheres (Schellart, 2000; Rossi & Storti, 2003; Abdelmalak *et al.* 2016), corundum (Panien *et al.* 2006), sugar (Schellart, 2000; Rosenau *et al.* 2009) and dry mortar (Gutscher *et al.* 1998).

Most studies investigating brittle deformation in upper crustal settings used granular materials, generally defined as cohesion-less frictional-plastic Coulomb materials (Huiqui *et al.* 1992; McClay, 1996; Costa & Vendeville, 2002). Among granular materials, quartz sand is the most applied, being relatively easy to use for the construction and sectioning of models and for its dynamic scalability. Mechanical tests showed that granular materials, rather than deforming as a Coulomb material with constant frictional properties, have a more complex strain-dependent behaviour (Krantz, 1991; Schellart, 2000; Marcher & Vermeer, 2001; Lohrmann *et al.* 2003; Adam *et al.* 2005; Panien *et al.* 2006), characterized by distributed pre-failure deformation, shear localization and strain accumulation in shear zones with reduced

https://doi.org/10.1017/S0016756821001321 Published online by Cambridge University Press

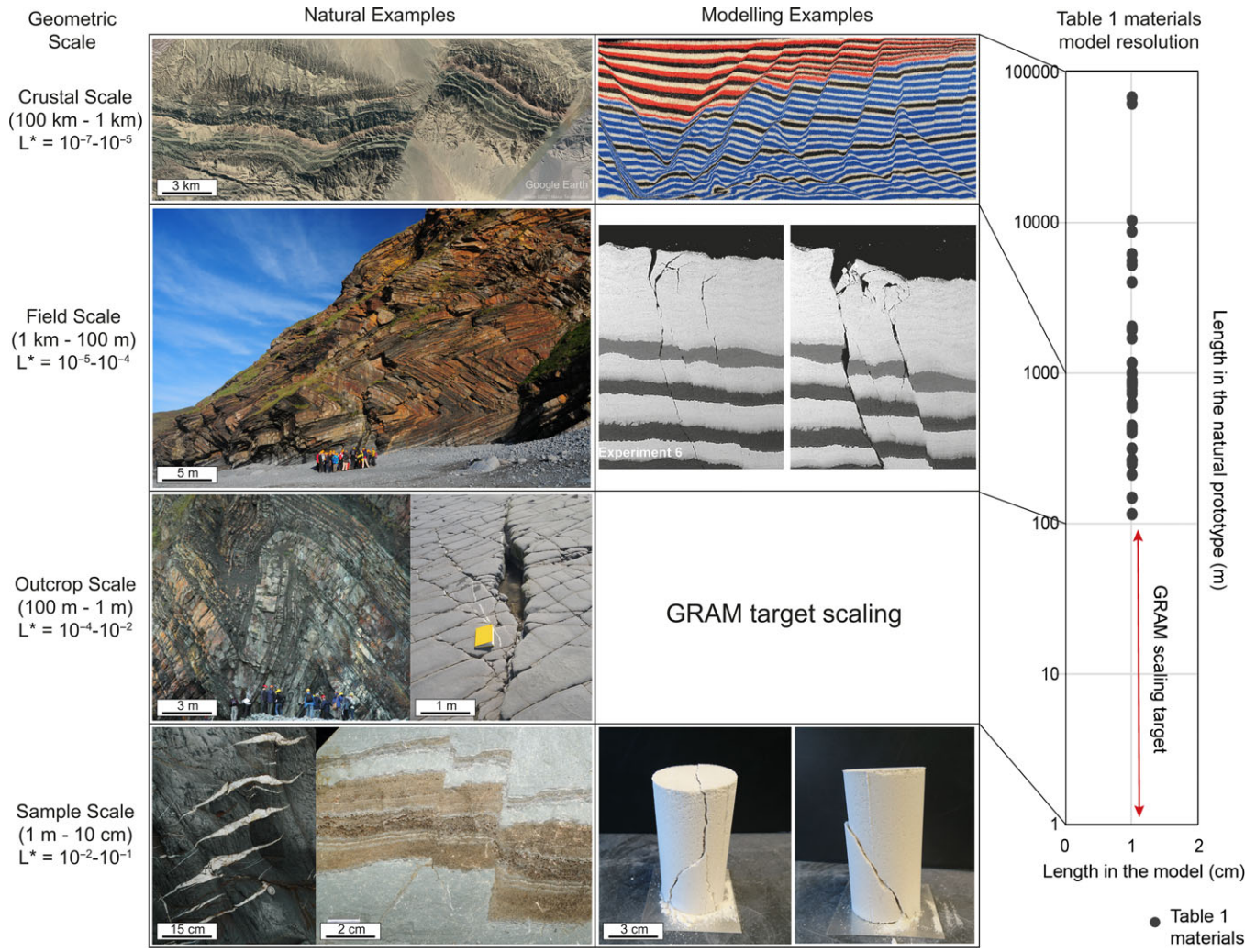

Fig. 3. Natural examples of geological structures observable at different scales; investigation methods (analogue modelling and mechanical tests) of geological processes at different scales; model resolution, in terms of length ratios model/prototype, provided by different model materials applied in tectonics studies (Table 1), calculated for the limestone of the Lueders Formation (15 MPa of cohesive strength and 2.43 g cm^{-3} of density; online Supplementary Table S1). Geometric scaling factor $L^* = L_n/L_m$. Photographs from ATML@RHUL, Google Earth and van Gent *et al.* (2010).

shear strength. The nonlinear behaviour of natural rocks in the brittle crust is therefore well simulated by granular materials (Fig. 4), because granular flow and brittle deformation are governed by similar material mechanics (Mandl, 1988; Marone, 1998).

The model materials used in some analogue modelling studies, with accessible cohesive strength and density values, are summarized in Table 1. The cohesive strength and density values range from 1 to 700 Pa and from 0.8 to 2.04 g cm^{-3}, respectively. We compared the geometric scaling factors of these model materials in the simulation of brittle deformation processes in upper crustal settings. For the length equivalence calculation, we used a limestone of the Lueders Formation as a natural prototype, with a cohesive strength of 15 MPa and density of 2.43 g cm^{-3} (see online Supplementary Table S1, available at http://journals.cambridge.org/geo).

The resulting geometric scaling factors are shown in Figure 3. It can be noticed that the presented model materials provide model resolution, in terms of geometric scaling factor, ideal for the simulation of crustal- and field-scale structures, but not suitable for the modelling of processes at the outcrop scale. To fill this gap of resolution relevant for fault zone and damage zone observations, the development of new rock-analogue material is therefore needed.

3. GRAM development

The development of a new GRAM capable of simulating fault–fracture processes at the resolution of the outcrop scale can fill the gap in model materials applied in analogue modelling studies. For this purpose, GRAM must be able to form shear and tensile fractures under variable stress conditions. It must therefore be a cohesive granular aggregate, with specifically scaled shear and tensile strength for the successful simulation of coupled fault–fracture processes in scaled analogue experiments. The developed material must maintain the frictional properties and granular flow characteristics of quartz sand with strain-dependent frictional properties, strain hardening and strain softening, dilatancy and shear strength (Krantz, 1991; Schellart, 2000; Lohrmann *et al.* 2003; Panien *et al.* 2006). The bulk granular material of the GRAM aggregates is therefore dry quartz sand of fine- to medium-sized grains (BL60, Prince Minerals Inc. Group).

https://doi.org/10.1017/S0016756821001321 Published online by Cambridge University Press

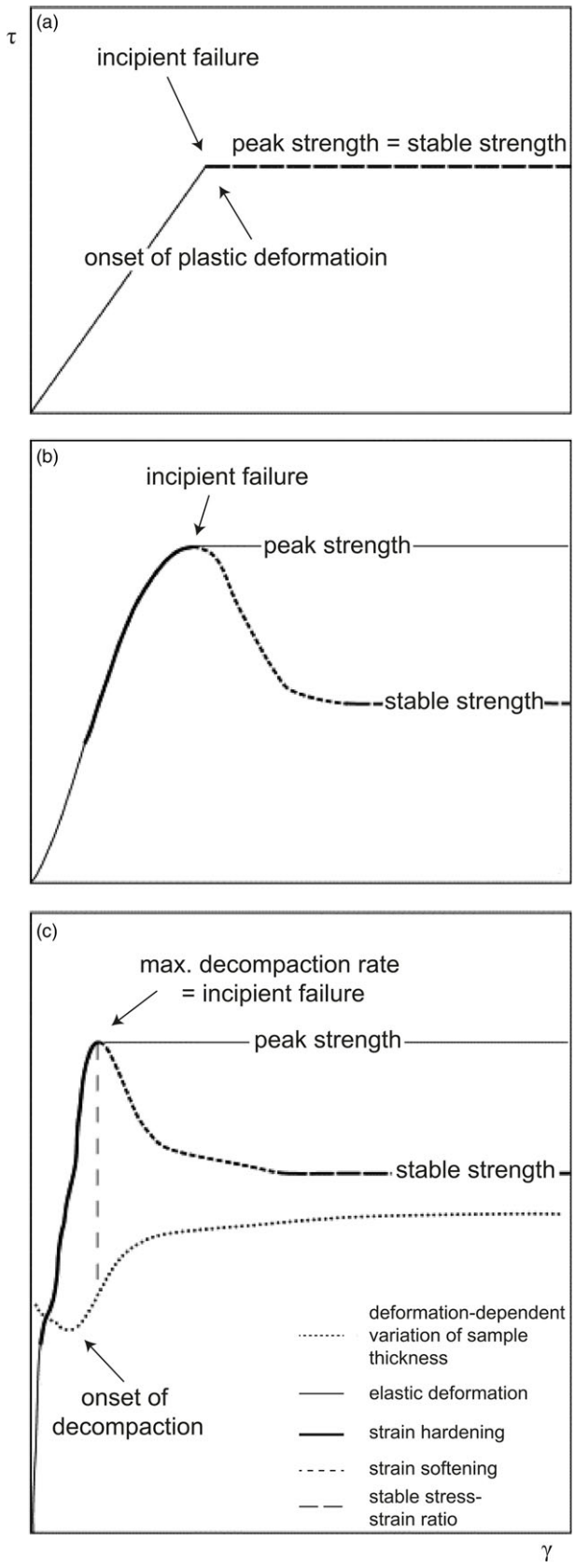

Fig. 4. Schematic shear stress (τ) versus angular shear (γ) curves showing the behaviour of (a) an ideal Coulomb material, and the similar nonlinear behaviour of (b) rocks in the brittle upper crust and (c) granular analogue materials (Lohrmann *et al.* 2003).

In this study, we have tested two approaches of material design with (1) dry cemented granular solids and (2) wet cohesive granular solids. To form cohesive sand aggregates comparable to an ultra-weak artificial sandstone, the sand particles were bonded either with (1) water-based (dry sand aggregates) or (2) fluid-based (wet sand aggregates) adhesive agents. Dry cemented granular solids were created with weak adhesives based on gelatine, hemihydrate and sugar-based components. Wet granular solids were created by flushing and draining sand aggregates with vegetable oil. The systematic variation of the bonding strength of the cemented sand aggregates, or the capillary forces in 'wet' sand aggregates, allows the calibration of the shear, compressional and tensile strength of the GRAM material.

The development of the sand aggregates followed a systematic workflow with a step-by-step assessment of the material characteristics. Only the sand aggregates fulfilling the required physical and mechanical properties of the initial qualitative assessment were taken forwards to the next level of material design and mechanical testing.

Finally, for a large-scale test, the best GRAM candidates were tested in a full-scale analogue experiment series in a simple shear strike-slip deformation rig to simulate the localization and growth of a strike-slip fault zone with a simple experiment set-up (see Section 5).

3.a. Material requirements

The material development was based on the following physical and mechanical requirements. GRAM must be capable of (1) forming cohesive aggregates with compositional and mechanical homogeneity on a sample and experiment scale; (2) deforming by shear and tensile failure under variable stress conditions; (3) preserving the frictional properties and granular flow characteristics of quartz sand with nonlinear elastic-plastic frictional behaviour, strain hardening and strain softening, dilatancy and shear strength (Krantz, 1991; Schellart, 2000; Lohrmann *et al.* 2003; Panien *et al.* 2006; Chemenda *et al.* 2011); and (4) providing the required dynamic scaling for the targeted fault–fracture processes resolution.

The aggregates were qualitatively tested in terms of handling and compositional homogeneity as part of the sample preparation procedure. Compositional irregularities can determine unfavourable physical and mechanical heterogeneities or anisotropies throughout the sample, conditioning the deformation during the experiments.

The candidate materials were also evaluated in terms of ease of preparation, sample reproducibility and application in analogue deformation rigs. Advanced studies (Schellart, 2000; Lohrmann *et al.* 2003; Panien *et al.* 2006; Klinkmüller *et al.* 2016; Schreurs *et al.* 2016) proved that the physical properties of the material, such as density, grain shape, pore space and grain size distribution, have an impact on their compaction behaviour and mechanical properties. Evidently, the sample preparation process represents a crucial step of the experiments since the manual procedure can have a direct impact on the properties of the aggregates, such as density and pore space distribution. Additionally, ambient laboratory conditions can influence the chemical reactions and moisture content of the samples. To maximize the accuracy of the sample reproducibility, a standardized sample preparation workflow is therefore required for each model material.

https://doi.org/10.1017/S0016756821001321 Published online by Cambridge University Press

Table 1. Overview of the studies and materials referred to for dynamic scaling comparison and related values of cohesive strength and density

Material	Cohesive strength C_m (Pa)	Density ρ_m (g cm^{-3})	Reference
Castor sugar	247	1.04	Schellart (2000)
Clay	50–140	1.55–1.65	Henza *et al.* (2010), Bonini *et al.* (2016), Bonanno *et al.* (2017), Hatem *et al.* (2017)
Corundum, brown	29–49	1.55–1.89	Panien *et al.* (2006)
Corundum, white	99–105	29–49	Panien *et al.* (2006)
Dry mortar	150	2	Gutscher *et al.* (1998)
Gelatin	6	1	van Dinther *et al.* (2013)
Gelatin–salted gelatin	1	1.1	Brizzi *et al.* (2016)
Glass fragments	35–41	1–1.24	Panien *et al.* (2006)
Glass microspheres	21–160	1.4–1.91	Schellart (2000), Panien *et al.* (2006), Abdelmalak *et al.* (2016)
Glass microspheres–silica powder	239–519	1.5–1.6	Abdelmalak *et al.* (2016)
Hemihydrate powder	31.35–200	0.73–0.9	Holland *et al.* (2006), van Gent *et al.* (2010), von Hagke *et al.* (2019)
Loess	200	1.3	Cobbold *et al.* (2001)
Microspheres (hollow, aluminium hydroxide)	6	0.39	Rossi & Storti (2003)
Microspheres (hollow, siliceous)	1.5	0.15	Rossi & Storti (2003)
Rice–sugar–rubber pellets	10	0.9	Rosenau *et al.* (2009)
Pyrex	4–10	0.97–1.09	Panien *et al.* (2006)
Sand	10–520	1.3–1.9	Krantz (1991), Gutscher *et al.* (1998), Bonini *et al.* (2000), Schellart (2000), Cobbold *et al.* (2001), Lohrmann *et al.* (2003), Panien *et al.* (2006), Gomes (2013), Wu *et al.* (2015), Dotare *et al.* (2016), Maestrelli *et al.* (2021), Santolaria *et al.* (2021)
Sand–barite	188.13	1.81	Gomes (2013)
Sand–cement	420	1.56–1.69	Krantz (1991)
Sand–clay	57.1–700	0.94–1.68	Krantz (1991), Gomes (2013),
Sand–hemihydrate	0–250	1.2–1.8	von Hagke *et al.* (2019), Poppe *et al.* (2021),
Silica powder	262–560	1.33–1.6	Galland *et al.* (2006), Abdelmalak *et al.* (2016)

The material capability to deform by shear and tensile failure was evaluated by qualitatively examining the samples in UCTs. Additionally, RSTs enabled a comparison of the deformation behaviour of GRAM aggregates with dry quartz sand and the calculation of the cohesive strength values needed to obtain the dynamic scaling.

3.b. Dynamic scaling

Following the dynamic scaling procedure, the geometrical scaling factor was derived, allowing us to evaluate the experiment resolution provided by the aggregates. The targeted geometrical scaling factor ($L^* = 10^4$–10^2) enables the simulation and observation of coupled fault–fracture processes with a model resolution relevant for fault damage zones observed on structural scales (1 cm in the model corresponding to a range of 1–100 m in nature).

According to Equation (2), the geometrical scaling factor is determined by cohesion and density ratios of analogue material and natural prototype. The density of the tested aggregates was determined by weighing different known volumes of the materials samples. As demonstrated for loose sand (Krantz, 1991), the preparation technique has an impact on certain material properties, including density. With granular aggregates, the material density is strongly influenced by the compaction applied during sample preparation. For all the tested aggregates, the samples were prepared by distributing and compacting the material manually to avoid the occurrence of irregularities and voids within the sample.

The cohesion was derived from ring-shear tests with variable loading conditions. Each test cycle was performed with different values of normal load that, along with the related critical shear stresses, define the failure envelope of the material. The obtained stress–strain curves allowed the derivation of the cohesive strength values.

3.c. Tested aggregates

Quartz sand BL60 (physical and chemical characteristics summarized in Table 2) represented the main component of the four potential GRAM aggregates. This dry granular material was systematically tested with the ring-shear tester, defining its frictional properties and providing a baseline for comparison with the four aggregates in examination. The annular ring-shear cell (Fig. 5) was filled with dry quartz sand and sifted at a constant rate from a fixed height to ensure a homogeneous material distribution.

https://doi.org/10.1017/S0016756821001321 Published online by Cambridge University Press

Table 2. Quartz sand BL60 technical data provided by the Prince Minerals Inc. Group, including the material physical specifics, typical chemical analysis and typical particle size distribution (dry sieving BS410 test sieves)

		Chemical analysis		Particle size distribution	
Property	Value	Oxides	Weight %	Microns	% Retained
Bulk density	1.5 g cm^{-3}	SiO_2	99.7	600	Nil
		TiO_2	0.03	425	0.1
		Al_2O_3	0.11	300	4.6
Hardness (Mohr scale)	7	Fe_2O_3	0.02	212	42.9
		K_2O	0.02	150	46.1
		CaO	0.03	106	5.7
Specific gravity	2.65	LOI	0.07 max	75	0.4
				<75	0.2

LOI – loss on ignition.

Four types of sand aggregates were tested with different cementing materials: sand–gelatine, sand–sugar, sand–vegetable oil and sand–hemihydrate. The aggregates specifics, including mixing ratios and drying procedure, are summarized in Table 3.

Although gelatine, sugar and vegetable oil have not been used in analogue modelling studies to form aggregates with sands, sand–hemihydrate aggregates were previously used by Haug *et al.* (2014) to simulate fragmentation in rock avalanches.

3.d. Sample preparation

The aggregates were prepared in samples of the different shapes required for mechanical tests. A standardized preparation workflow was defined for each aggregate to ensure their reproducibility and to reduce the impact of ambient conditions and operator handling.

For sand–gelatine, sand–sugar and sand–hemihydrate aggregates, a certain amount of water was added to dissolve the solute, gelatine and sugar or, in the case of hemihydrate powder, to amalgamate with sand. For sand–vegetable oil aggregates, an addition of flour completed the mixture. The sample preparation and the drying-up phases were performed at controlled ambient laboratory conditions.

The drying-up time can have an impact on the material mechanical properties as a result of the variable moisture content of the samples. Sample moisture content was therefore analysed by time-series data of the sample weight in 24-hour intervals to monitor water loss.

For ring-shear tests, the samples were prepared and dried directly in the ring-shear cells (942.48 cm^3 volume, 10 cm inner diameter, 20 cm outer diameter and 4 cm height). The cylindrical test samples for uniaxial compression tests were prepared and dried in steel moulds (100 mm height and 50 mm diameter).

Sand–gelatine aggregates were prepared using food gelatine HI 250 Bloom, dissolved in boiling water at a proportion of 1:20. The solution was poured on the sand samples until saturated. Finally, the samples were dried under laboratory conditions for 18 hours.

Sand–sugar aggregates were prepared by immersing the sand cylindrical samples into a solution of sugar and water for variable

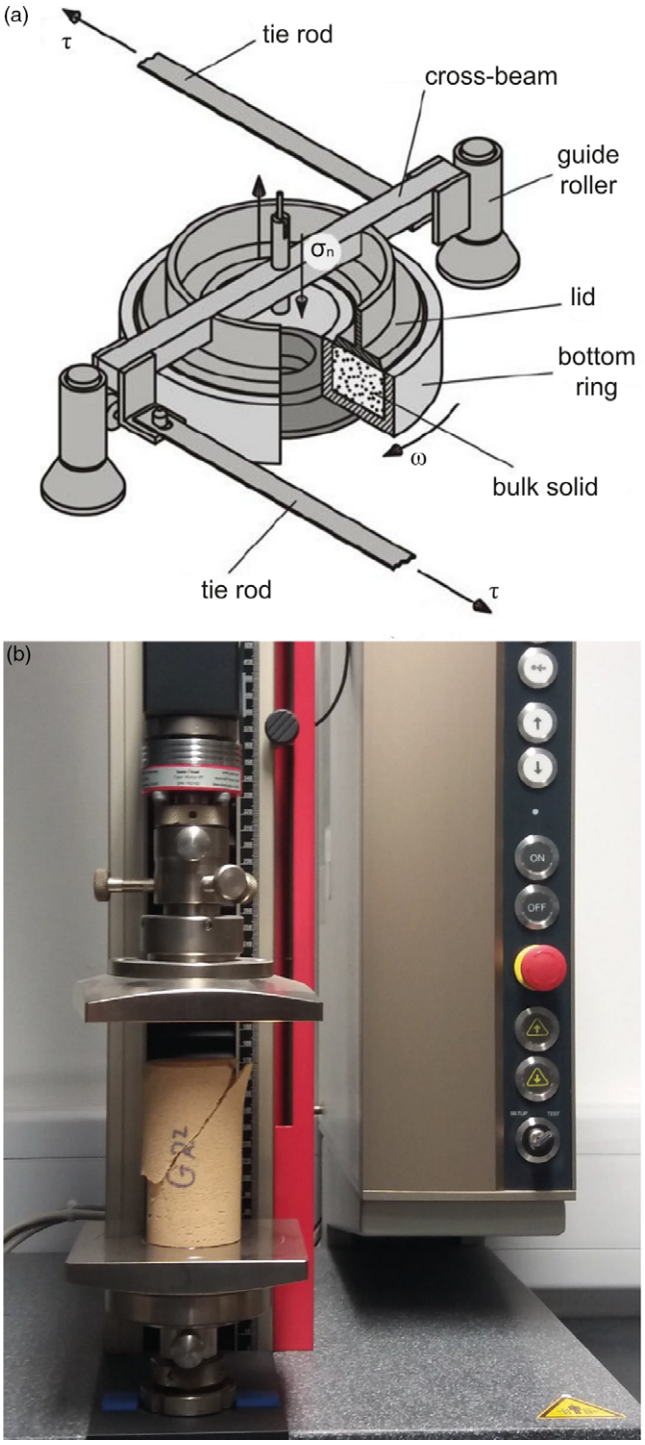

Fig. 5. Mechanical testers used in this study: (a) ring-shear tester sketch (modified after Schulze, 1994) and (b) uniaxial compression tester.

times (tested from 5 to 30 minutes) sufficient to ensure saturation throughout the sample. The water–sugar solution was also tested with different concentrations of solute, from 10 to 100 g L^{-1}. The drying procedure was evaluated at different conditions and duration, from 8 to 18 hours in the oven and from 5 to 7 days at laboratory conditions.

Sand–vegetable oil samples were prepared by mixing the two components together with the addition of flour (55% of quartz sand, 33% of flour and 12% of vegetable oil). These aggregates

https://doi.org/10.1017/S0016756821001321 Published online by Cambridge University Press

Table 3. Summary of the aggregates tested in this study

Aggregate name	Adhesive agent	Other additions	Materials proportion	Drying phase
Sand–gelatine	Food gelatine	Water	50 mL/L added until saturation	18 hours
Sand–sugar	Caster sugar	Water	10–100 g/L added until saturation	8–18 hour oven or 5–7 days air-dried
Sand–vegetable oil	Vegetable oil	Flour	55% sand, 33% flour, 12% oil	Not required
Sand–hemihydrate	Hemihydrate calcium sulphate	Water	1%, 2%, 3% and 4% hemihydrate	4–6 days

Table 4. Requirements checklist of the tested materials

	Sample preparation			Uniaxial compression test	Ring-shear test	
Material	Form aggregates	Handling issues	Sample homogeneity	Shear and tensile fractures	Nonlinear behaviour	Target scaling
Sand–gelatine	✓	✗				
Sand–sugar	✓	✓	✗			
Sand–vegetable oil	✓	✓	✓	✗	✓	✗
Sand–hemihydrate	✓	✓	✓	✓	✓	✓

did not require the addition of water, so therefore excluded the drying procedure from the sample preparation workflow.

Sand–hemihydrate aggregates were examined at different mixing ratios, with 1%, 2%, 3% and 4% of hemihydrate calcium sulphate powder ($CaSO_4{\cdot}½H_2O$). The samples were prepared by mixing the dry parts first, accurately separating the particle agglomerates and obtaining a homogeneous mixture. The water was gradually added to the mixture (10% of the total weight) under continuous stirring. The samples were air-dried at laboratory conditions for 4–6 days.

3.e. Material mechanical testers

The mechanical properties of the aggregates, including frictional parameters, cohesion, shear and compressive strength, were determined by means of RSTs and UCTs.

The dynamic ring-shear tester (Schulze, 1994), specially designed for powder testing, enables the analysis of shear properties under low normal loads in the range of the stresses observed in scaled analogue experiments (Lohrmann *et al.* 2003). The stress–strain curves of the examined aggregates were analysed under variable normal loads to determine their dynamic frictional parameters, cohesion, shear strength and dilatancy. The shear tester is composed of a stainless-steel ring-shaped cell where the tested material is placed, a lid, two tie rods and a crossbeam (Fig. 5a). Through the lid, fitting on top of the filled cell and counterbalanced by a weight, a normal load is applied to the sample. A horizontal shear force is applied by the cell rotation, occurring at a constant angular velocity, during which the lid is fixed with tie rods and a crossbeam to the strain gouges. The lid is anchored into the sample by means of several steel protrusions, ensuring shear inside the sample itself and avoiding slipping between material and lid. Measurements were performed with different normal loads ranging from 1 to 20 kPa. For each measurement, the stress–strain curve was measured for the undeformed and then deformed material in two successive shear cycles (Lohrmann *et al.* 2003).

A tensional–compressional uniaxial tester (Zwicky 5N, Zwick Roell) was used to analyse the elastic properties and compressive strength of aggregates under uniaxial loading. The tester is composed of a plate where the sample is placed and uniaxially compressed by a vertical load applied by a servo-controlled piston (Fig. 5b). During the test, the cylindrical samples, with a length: diameter ratio of 2, undergo deformation until breaking, allowing the analysis of the failure modes of the materials. The test can be performed either in load-controlled or strain-controlled conditions and the applied force (N) and occurring deformation (%) are measured.

4. GRAM test results

Following the material requirements of GRAM (Section 3.a above), the tested aggregates were examined in a step-by-step workflow, where only the suitable aggregates were further tested at the next stage (Table 4).

4.a. Sample preparation

During sample preparation, the suitability of sand mixtures was assessed to form cohesive aggregates with compositional homogeneity.

Gelatine-based aggregates were characterized by moisture-dependent properties, considerably increasing in strength over time. The samples showed diffuse deformation under wet conditions, whereas the samples were too strong to be tested by UCT (maximum uniaxial load of the tester: 5000 N) when completely dry (after about 18 hours of drying-up), showing a highly time-dependent cohesion. Due to this complexity in material handling, sand–gelatine aggregates were excluded.

Sand–sugar aggregates were unsuitable to produce homogeneous samples in all the different mixing ratios and drying-up procedures tested. The aggregates developed sugar crusts on the outer part of the sample and maintained loose sand volumes inside. For this reason, sand–sugar aggregates were excluded from the successive tests.

Sand–vegetable oil and sand–hemihydrate aggregates formed cohesive and homogeneous samples, showing no handling issues, and were therefore taken to the next stage of tests. For these two aggregates, the sample preparation workflows were defined including mixing procedures, ratios and drying time.

https://doi.org/10.1017/S0016756821001321 Published online by Cambridge University Press

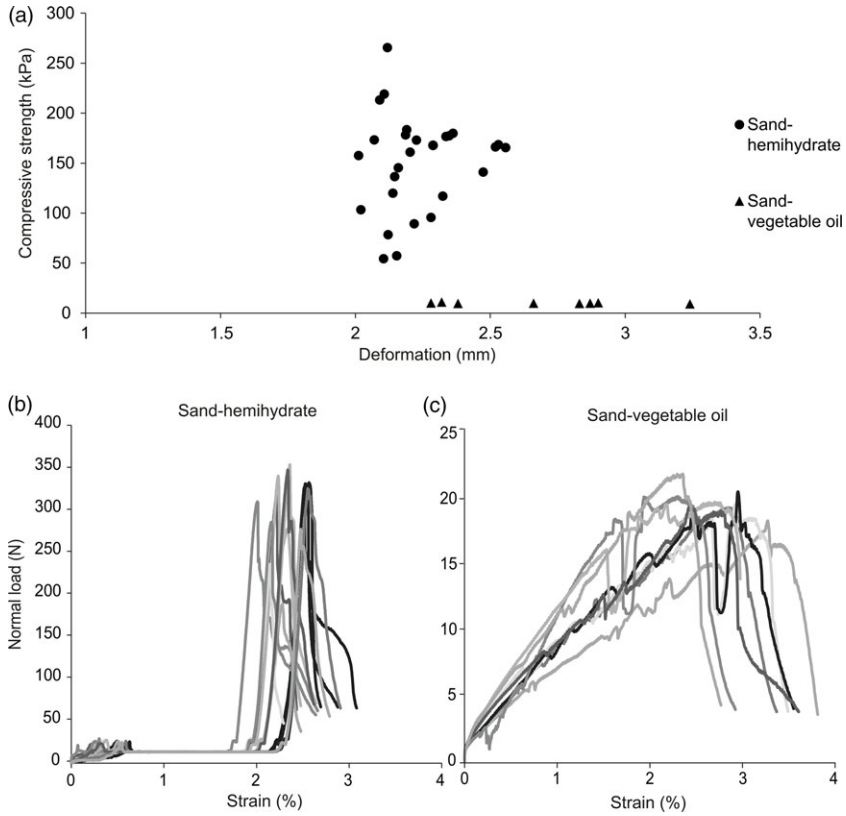

Fig. 6. Uniaxial compression test results for sand–hemihydrate and sand–vegetable oil samples: (a) compressive strength derived from the tests and (b, c) normal load (N) versus strain (%) curves.

4.b. Uniaxial compression tests

The capability of the aggregates to simultaneously deform by shear and tensile failure was qualitatively analysed by means of a tensional–compressional uniaxial tester. From the quantitative point of view, the UCT series allowed the elastic properties and compressive strength parameters of the materials to be determined.

At this stage, only sand–vegetable oil and sand–hemihydrate aggregates were tested. The compressive strength, calculated for each specimen as the normal load (N) per unit area at failure, showed higher values for sand–hemihydrate aggregates than for sand–vegetable oil samples (Fig. 6a). The latter exhibited a more diffused deformation with higher deformation rates, as shown by the UCT normal load/strain curves (Fig. 6b).

At failure, sand–vegetable oil aggregates mainly deformed by distributed shear fractures (Fig. 7), usually developing a single shear fracture. On the other hand, sand–hemihydrate aggregates localized the deformation by shear and tensile failure (Fig. 7), developing patterns of early micro-cracks linking together in macro-fractures by coalescence with increasing loading stresses. The specimens usually showed multiple fracture planes, with the main fractures spanning through the whole sample. As a result of this qualitative test, sand–vegetable oil aggregate was considered unsuitable for this study purposes. This material was tested in RST series for comparison purposes only.

4.c. Ring-shear tests

In order to evaluate the strain-dependent deformation behaviour and frictional parameters of the GRAM aggregates, the samples were tested with the ring-shear tester and compared with the baseline stress–strain curves of BL60 dry quartz sand.

Ring-shear tests were performed for sand–hemihydrate and sand–vegetable oil aggregates. In the comparison of the stress–strain curves (Fig. 8), the nonlinear elastic–plastic frictional behaviour, with strain hardening and strain softening, was observed in both tested aggregates, preserving this granular materials characteristic. Quantitatively, sand–hemihydrate aggregates showed higher shear strength (peak, static and dynamic) and strain softening than sand–vegetable oil and loose sand samples. Sand and sand–vegetable oil samples showed very similar peak strength values. In detail, the shear stresses required for shear failure in sand–hemihydrate aggregates at a normal stress of 10 kPa was about 14% and 18% higher than loose sand and sand–vegetable oil aggregates, respectively.

Cohesion values for each tested material were extrapolated by plotting the critical shear and normal stresses in a Mohr diagram (Fig. 9). The best-fit linear failure envelopes were calculated. The obtained parameters, including cohesion, coefficient and angle of internal friction, are summarized in Table 5.

4.d. Dynamic scaling

As mentioned above (Section 2.c.1), for a dynamically scaled model the analogue material must have rheology and angle of internal friction similar to the natural prototype. Following RSTs, sand–vegetable oil and sand–hemihydrate samples yielded values for the angle of internal friction of 33 and 37°, respectively (Table 5). Additionally, to calculate the geometric scaling factor that the material can provide in scaled experiments, density and cohesion parameters of model material and natural rocks are needed. The dynamic scaling parameters are summarized in Table 6.

Sand–vegetable oil aggregates showed cohesion values of 291 Pa, whereas sand–hemihydrate aggregates had cohesion values one order of magnitude higher, namely 7883 Pa.

https://doi.org/10.1017/S0016756821001321 Published online by Cambridge University Press

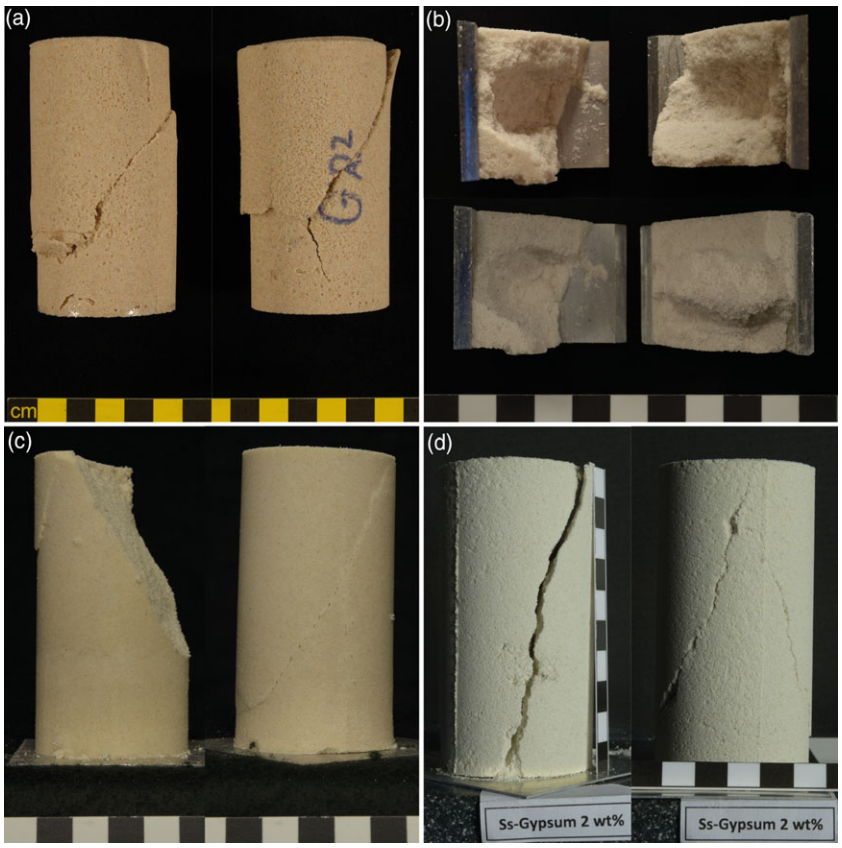

Fig. 7. Samples after uniaxial compression tests: (a) sand–gelatine; (b) sand–sugar; (c) sand–vegetable oil; and (d) sand–hemihydrate.

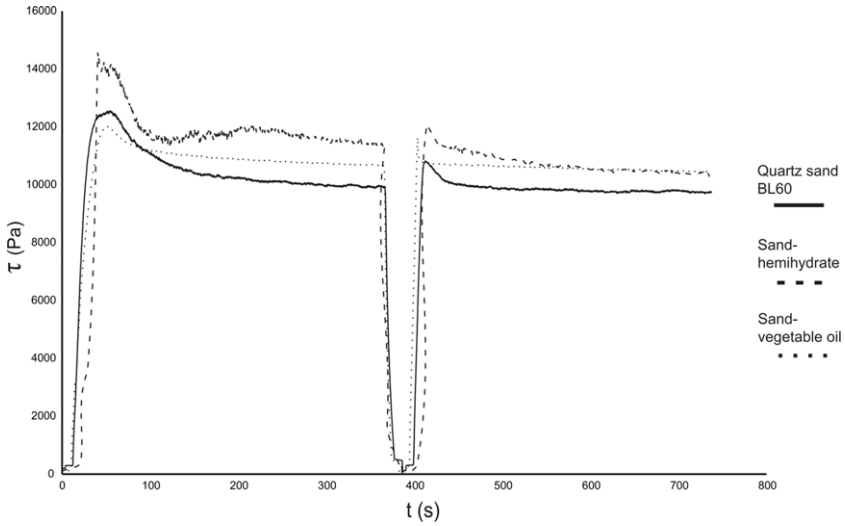

Fig. 8. Ring-shear test diagrams (shear stress versus time) for sand–hemihydrate, sand–vegetable oil samples and quartz sand BL60.

The density of sand–vegetable oil aggregates was calculated by weighing the RST samples with known cell volume and weight, providing values of 1.52 g cm^{-3}. In the case of sand–hemihydrate samples, the drying stage and the related samples moisture content made the density values more uncertain. To obtain a better estimation of the sand–hemihydrate density, it was calculated by weighing different sample volumes including the samples prepared for the strike-slip experiments and for the mechanical tests, namely the cylindrical specimens for uniaxial compression tests and the two cells used for ring-shear tests. The slope of the linear regression line provided the best estimate of density of 1.36 g cm^{-3} (Fig. 10).

From the obtained cohesion and density values, the geometric scaling factor has been calculated by using Equation (2) and reference natural rocks with known cohesion and density values (Lueders Formation limestone used for comparison; Fig. 3; 15 MPa and 2.43 g cm^{-3}). The length equivalence for sand–vegetable oil and sand–hemihydrate was 1 cm in the model corresponding to 322.43 and 10.65 m in nature, respectively. Only the dynamic scaling provided by sand–hemihydrate aggregates therefore fitted the outcrop scale, enabling an ideal model resolution to simulate fault and fracture processes at the structural scale. By comparison with the model materials used in analogue modelling studies

https://doi.org/10.1017/S0016756821001321 Published online by Cambridge University Press

Table 5. Summary table of cohesion (Pa), angle of internal friction ϕ (°) and coefficient of internal friction μ (dimensionless) obtained after ring-shear tests for loose sand 'BL60', sand-vegetable oil aggregates and sand-hemihydrate aggregates. The error is the standard deviation of the mean values after multiple measurements (4 cycles of 5 tests each)

Material	Cohesion (Pa)	Angle of internal fiction ϕ (°)	Coefficient of internal friction μ (–)
Sand BL60	13 ± 1.23%	36.55 ± 1.23%	0.74 ± 1.23%
Sand–vegetable oil	291 ± 4.78%	33.4 ± 3.1%	0.66 ± 3.1%
Sand–hemihydrate	7883 ± 5.75%	37.1 ± 2.69%	0.76 ± 2.69%

Table 6. Dynamic scaling parameters calculated for sand BL60, sand–vegetable oil and sand–hemihydrate aggregates. Model resolution (L_n) corresponding to 0.01 m in the model (L_m)

Material	Cohesion (Pa)	Density ρ (g cm^{-3})	Geometrical scaling factor L^*	Model resolution L_n (m)
Sand BL60	13	1.5	1.4×10^{-6}	7123
Sand–vegetable oil	291	1.52	3.1×10^{-5}	322
Sand–hemihydrate	7883	1.36	9.39×10^{-4}	10.65

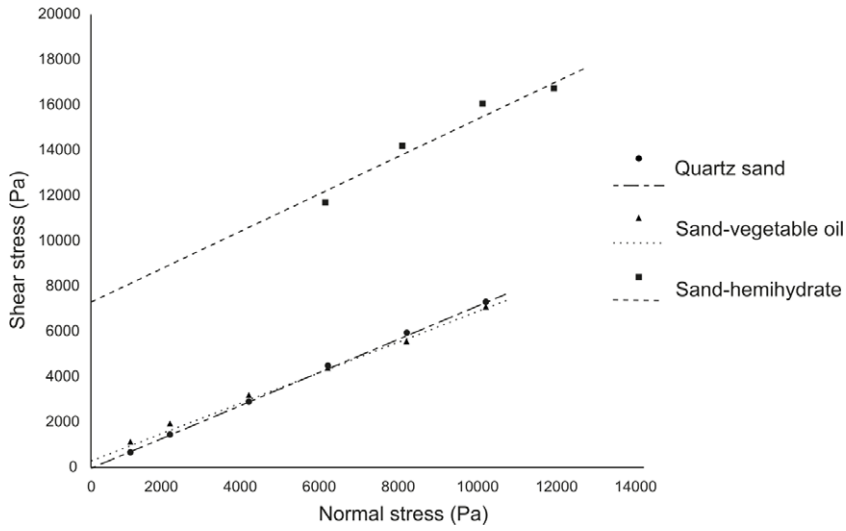

Fig. 9. Mohr diagram showing the shear stress as a function of the normal stress for quartz sand BL60, sand–vegetable oil aggregates and sand–hemihydrate aggregates.

(Fig. 3), the developed sand–hemihydrate material filled the gap of resolution corresponding to the outcrop scale.

5. GRAM strike-slip experiment

In Sections 3 and 4 we developed a GRAM prototype with required mechanical and physical properties for the simulation of coupled fault–fracture processes in scaled experiments, and have tested its sample-scale preparation and mechanical properties. The next step is to demonstrate the application of GRAM in scaled experiments simulating the localization and growth of coupled fault–fracture processes. For this purpose, the material was prepared in large volumes and applied in strike-slip experiments.

The strike-slip setting was chosen for its simple set-up and ideal orientation for strain analysis, with the shear zone evolution being observable in map view on the sample surface by stereo DIC techniques. This type of experiment, usually referred to as the Riedel experiment, simulates the deformation in an overburden lying on a straight and vertical basement fault (Cloos, 1928; Riedel, 1929) and has been performed with a large variety of model materials (Dooley & Schreurs, 2012).

The experiments were monitored by 3D stereo DIC techniques, which enabled the high-resolution monitoring of the 3D surface displacement and deformation of the experiment surface for the fully quantitative analysis of dynamic fracture localization and crack propagation in the experiment.

The experiment series confirmed that GRAM aggregates can be prepared and handled in large experiment volumes. Furthermore, the structural-scale fracture processes and fault localization observed in the experiments presented the characteristic elements of large-scale fault localization and early fault zones evolution. Finally, DIC analysis provided insights into the dynamic evolution of a fault damage zone at the relevant structural scale.

5.a. Experiment set-up

The experiments were performed with a 100-cm-long, 60-cm-wide and 12-cm-high strike-slip rig (Fig. 11). The apparatus simulated the shear deformation in a horizontal material layer overlying a straight strike-slip fault. The base of the rig consisted of two mobile metal baseplates with a linear central interface representing a single planar and vertical basement fault. The baseplates were able to

https://doi.org/10.1017/S0016756821001321 Published online by Cambridge University Press

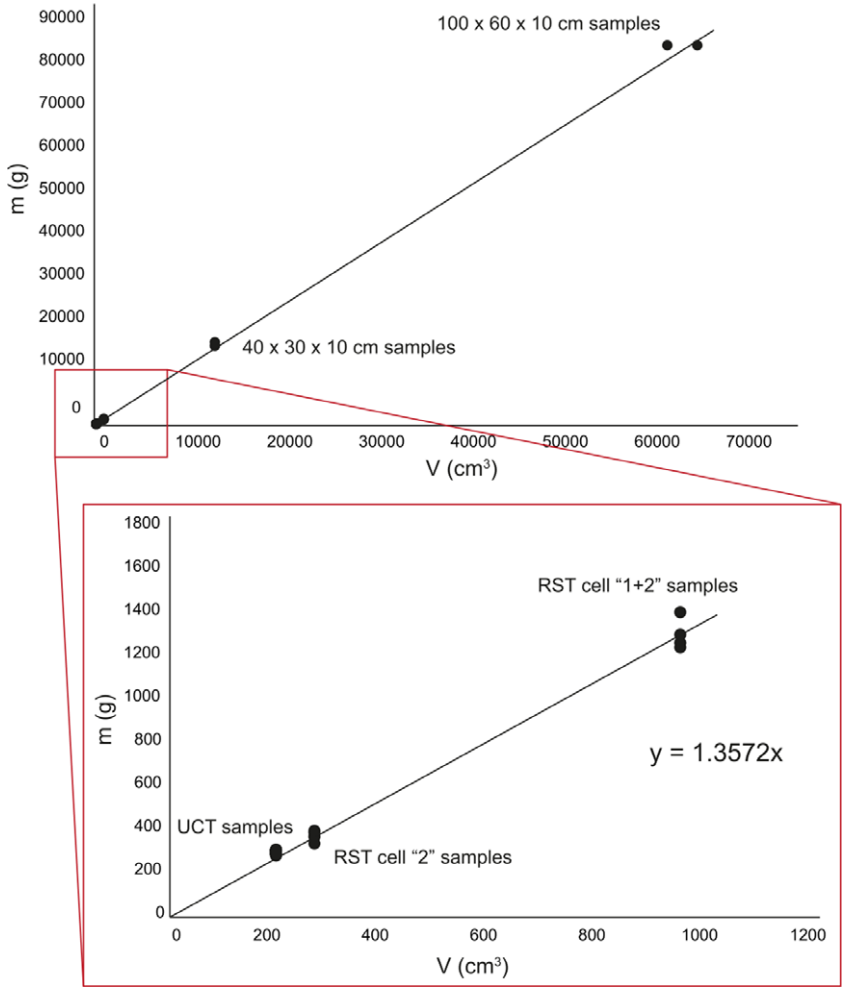

Fig. 10. Plots of mass versus volume for sand–hemihydrate model material.

translate independently parallel to the strike direction of the central velocity discontinuity, that is, the fault interface. The 12-cm-high rig walls were in place during the sample preparation and confined the model during deformation. The displacement was manually applied to the baseplates by a hydraulic winch attached to the rig because the application of standard electric stepper motors used in dry sand shear experiments was prevented by the high strength of the GRAM. The deformation was applied by moving one of the two baseplates with a shear sense arbitrarily chosen to be dextral. The basal interface consisted of two separate 1-mm-thick metal baseplates, each of which was covered with a glued-on rubber sheet, forming a high-friction basal interface with the sample aimed at minimizing slippage on the rig base.

A total of nine strike-slip experiments were performed with the sand–hemihydrate GRAM (see online Supplementary Table S2, available at http://journals.cambridge.org/geo). The new GRAM was prepared for an initial set of experiments in smaller volumes (40 × 30 × 10 cm) and adjusted for the later set of experiments in significantly larger volumes (100 × 60 × 10 cm) to minimize the impact of edge effects of the experiment set-up on the fault damage zone evolution. GRAM at 3% wt of hemihydrate was applied in the first three experiments, whereas GRAM at 2% wt was applied in the successive six experiments (see online Supplementary Table S2). The first pilot experiments allowed the evaluation of various sample preparation issues, such as the drying-up of large material volumes, their handling and the experiment set-up specifics.

In the smaller experiments (1–4), the influence of significant boundary conditions as a result of the relatively small sample dimensions was highlighted. Fractures initiated at the velocity discontinuity of the sample–rig walls and propagated to the central sample area, therefore influencing the damage zone localization and evolution (Fig. 12a). This edge effect was limited by increasing the sample dimensions to 100 × 60 × 10 cm, enabling the shear zone to localize and develop in the model without being impacted by the 'boundary effect' fractures (Fig. 12b).

The material volumes were prepared following the sample preparation workflow defined for the mechanical tests (Section 3.d above). For the 40 × 30 × 10 cm samples *c.* 18 kg of dry materials were used, whereas the 100 × 60 × 10 cm samples required *c.* 80 kg. The smaller experiment volumes were prepared and dried in a wooden box with detachable walls and subsequently transferred to the rig for the experiment. The larger experiment volumes were prepared and dried directly on the rig, reducing the risks of damaging the large sample during its relocation after the preparation and drying procedures. For the larger material volumes, the three components (sand, hemihydrate and water) were mixed in a concrete mixer. The mixture was transferred to the rig, accurately distributing the material by hands. Once all the material was in place within the rig walls, a wooden plate was positioned on top of the sample with weights (*c.* 100 kg) for *c.* 1 hour, ensuring material compaction. The sample height was 2 cm less than the rig walls to accommodate the compaction plate during the sample

https://doi.org/10.1017/S0016756821001321 Published online by Cambridge University Press

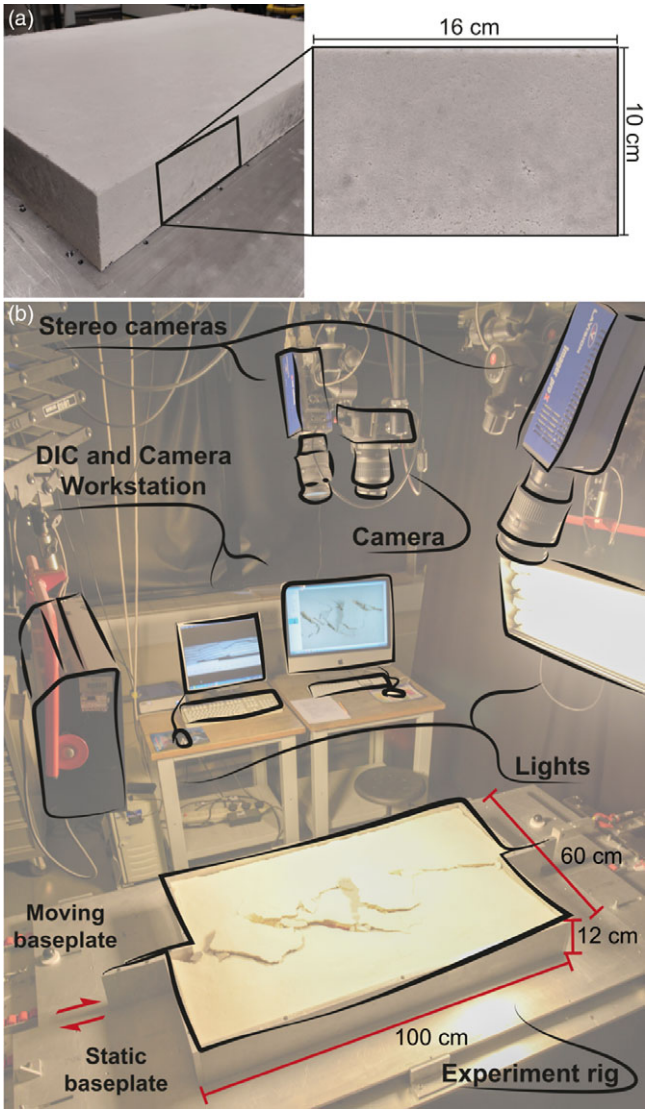

Fig. 11. Experimental set-up with 3D optical strain monitoring. (a) 100 × 60 × 10 cm sample with the rig walls removed to enhance the drying procedure. The sample shows a suitable level of homogeneity. (b) Laboratory set-up with stereoscopic CCD cameras and DIC set-up, with schematic representation of the strike-slip rig.

preparation. With this procedure, no voids or irregularities were observed throughout the samples, enabling a suitable level of material homogeneity (Fig. 11a).

The experiment series was performed with the described strike-slip rig set-up. As a representative experiment, GRAM test-7 was analysed and discussed in the following. The total shear displacement applied was 7 cm with an experiment duration of 17 minutes, resulting in an average slip rate of 4.12 mm min^{-1}.

The scaling factors of the experiment GRAM test-7 are summarized in Table 7, referring to the same prototype used for comparison (Fig. 3), namely the Lueders Limestone Formation (see online Supplementary Table S1). The length equivalence was 1 cm in the model corresponding to 10.65 m in the natural prototype.

5.b. Experiment monitoring

Digital Image Correlation (DIC) analysis techniques were applied for high-resolution strain monitoring in the GRAM strike-slip experiments (Adam *et al.* 2002, 2005, 2013*a*; Krézsek *et al.* 2007; Dotare *et al.* 2016). DIC analysis enables the full-field measurements of heterogeneous displacement, strain and porosity changes, as well as the monitoring of localized and diffuse deformation processes in the model from the large experiment scale to the particle scale with sub-millimetre accuracy (White *et al.* 2003; Adam *et al.* 2005; Viggiani & Hall, 2008). For the acquisition and analysis of sequential stereo images, we used the digital image correlation and deformation analysis software (Strain Master, LaVision) adapted for scaled analogue experiments. The monitoring equipment consisted of two high-resolution charge-coupled device (CCD) cameras in stereoscopic set-up above the experiment (Fig. 11b). From the ortho-corrected stereo images, the 3D experiment surface was calculated by means of a mathematical mapping function derived from 3D volume correlation and correction. For this purpose, a calibration plate with equidistant cross marks was placed on the entire sample surface; stereo images recorded the different positions of the calibration plate and allowed the derivation of the mapping function from the ortho-corrected calibration plate images. The volume correlation enabled the accurate 3D mapping of the experiment surface during deformation, and the subsequent calculation of the 3D incremental displacement vector field from successive time-series images, by digital image correlation. Finally, from the 3D displacement field, additional surface deformation displacement and strain components were calculated.

5.c. Experiment results

Here we show the results of GRAM test-7 experiment (parameters summarized in Table 8). The displacement and strain components, computed from the incremental DIC displacement field data of the experiment surface, enabled the kinematic and dynamic analysis of the shear zone evolution. These include the displacement field (mm), the shear strain ϵ_{xy} (%) and the vertical displacement (mm) derived from the incremental 3D displacement vector data (see online Supplementary Videos V1–V4, available at http://journals.cambridge.org/geo). These attributes were calculated incrementally for each time step ($\Delta t = 1$ s). Incremental displacement, shear strain and the *z*-displacement representing active deformation between subsequent time-series stereo images and derived displacement, shear strain and *z*-displacement rates are shown at six experimental stages, along with ortho-corrected surface images and the structural maps of the interpreted structures (Fig. 13). In the colour maps of incremental vector length (Fig. 13c–e), linear and sharp colour contrasts represent fracture localization and localized displacement of shear fractures. In the incremental DIC displacement field data (Fig. 13c–e), the fault localization is usually revealed before it can be observed in the raw images (Fig. 13a).

With this experiment set-up, only one of the two baseplates was translated with the static block of the sample (top part of map view in Fig. 13) mostly showing lower displacement and strain rate values.

The experiment showed the formation of a strike-slip shear zone from early localization of the first synthetic Riedel shears (R shears), striking *c.* 22° clockwise with respect to the trace of the basement fault, to their complete linkage into a continuous and anastomosing primary deformation zone (PDZ). The final damage zone developed asymmetrical to the basement fault as a result of the set-up consisting of a static and a moving baseplate. The total displacement applied to the rig was *c.* 7 cm, corresponding to *c.* 74.55 m in nature.

https://doi.org/10.1017/S0016756821001321 Published online by Cambridge University Press

Table 7. Dynamic scaling properties of the GRAM strike-slip experiments. Natural prototypes displacement rates from Mouslopoulou *et al.* (2009)

Quantity	Experiment (model)	Nature (prototype)	Scaling Factor
Length	1 cm	10.65 m	$L^* = \frac{L_m}{L_n} = \frac{C_m}{C_n}\frac{\rho_n}{\rho_m}\frac{g_n}{g_m}$ $L^* = 9.39 \times 10^{-4}$
Cohesion	7.88 kPa	15 MPa	
Density	1.36 g cm^{-3}	2.43 g cm^{-3}	
Gravity acceleration	9.81 m s^{-2}	9.81 m s^{-2}	
Internal friction coefficient	0.75	0.53	*c.* 1
Internal friction angle	37°	28°	*c.* 1
Displacement rate	*c.* 4.12 mm min^{-1}	0.08–2.83 mm a^{-1}	$7.64 \times 10^5 - 2.82 \times 10^7$
Stress	7.88 kPa	15 MPa	$\sigma^* = \frac{\sigma_m}{\sigma_n} = \rho^* g^* L^*$; $\sigma^* = 1.8 \times 10^{-4}$

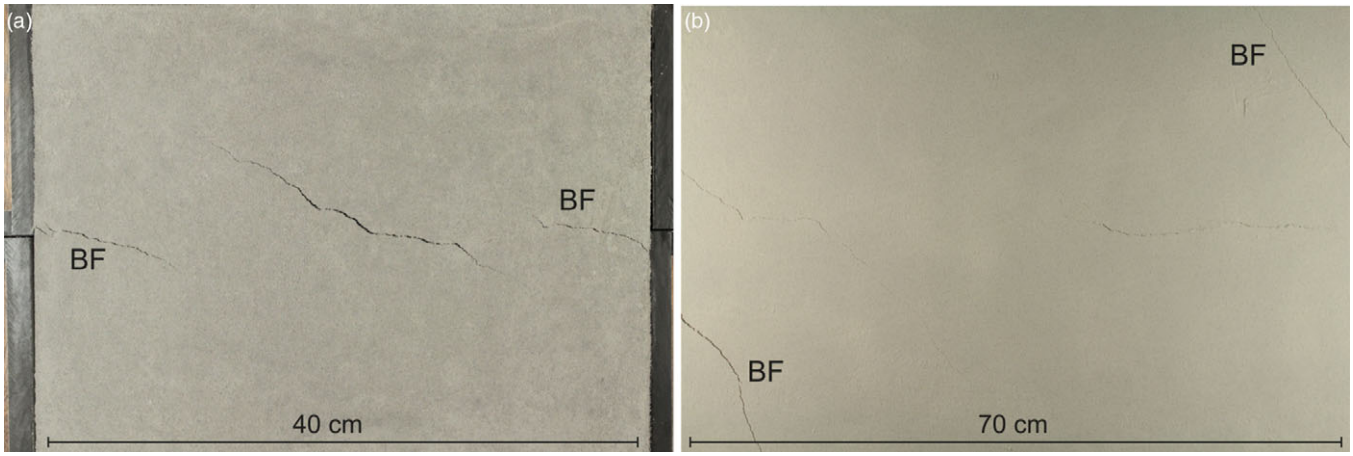

Fig. 12. Boundary effect of the rig walls on the samples with dimensions of (a) 40 × 30 × 10 cm and (b) 100 × 60 × 10 cm. BF – boundary effect fracture.

Mainly R and Y shears developed during the experiment, with only three R' shears clearly observed and characterized by limited activity; no P shears were identified. The Y shears in the lower part of the model (corresponding to the moving baseplate) localized as individual shears first and then linked to the earlier R shears. In the upper part of the model (corresponding to the static baseplate), the Y shears formed as part of the early R shears, and propagated towards the outer zones of the PDZ at lower angles. Tens of tensile fractures formed, mainly in the overlap areas between the main R shears or due to block uplift, rotation and failure. The open fractures and areas of local extension mainly corresponded to the right-lateral bends and step-overs of the fault traces.

In the final stages of deformation (30–40 mm displacement), active displacement was mainly accommodated by a single through-going strike-slip fault. At the same time, the intense early segmentation in the damage zone created small, 2–5-cm-long, discrete blocks or shear lenses, which underwent rotation and uplift obliterating the surrounding fault traces. Consequently, from this stage onwards no further new structures developed in the PDZ and, for this reason, we analyse the model evolution up to the 40-mm-displacement stage (Fig. 13).

In the six deformation stages shown in Figure 13c, the maximum displacement rate of observed shear fractures ranged from 0.11 to 1.4 mm s^{-1}. The highest rate was reached once the PDZ was completely interconnected, and all the displacement was accommodated by a through-going strike-slip fault.

The shear strain maps (Fig. 13d) show the shear sense of the different faults and fractures. The incremental shear strain (%) increases from the initial to the final stages, spanning ±0.85%, with the positive strain values (warm colours) indicating dextral shear sense and the negative values (cold colours) indicating sinistral shear sense (Fig. 13d). In general, the shear strain observed during the experiment is mostly dextral as the imposed rig sense of shear. Only a limited antithetic shear deformation was observed, with low or negligible negative values developed, and only three R' shears were observed.

The maps of incremental *z*-displacement visualize the vertical movements of fault blocks, including local pop-up structures, subsidence areas and thrust faults (Fig. 13e). The *z*-displacement rates (mm s^{-1}) of individual fault blocks is variable and ranges from −0.15 to 0.28 mm s^{-1}, with the positive values (warm colours) indicating uplift and the negative values (cold colours) indicating subsidence. In the first three experiment stages, the *z*-displacement rate is more distributed and mainly accumulated along fault traces, especially in the central area between early Riedel shears. In later stages, vertical displacement describes smaller discrete blocks undergoing uplift, rotation and, in only a few areas, local subsidence due to block fragmentation. The *z*-displacement also highlighted the occurrence of compressive areas, usually related to the left-lateral bends of the fault traces, additionally characterized by a strike-slip component.

In general, dextral strike-slip component was predominant over the reverse dip–slip movement. The maximum damage zone width

https://doi.org/10.1017/S0016756821001321 Published online by Cambridge University Press

Table 8. Specifics of GRAM test-7 strike-slip experiment

GRAM test-7 Experiment	
Model material	Sand–hemihydrate 2%
Sample dimension	100 × 60 × 10 cm
Initial set-up	Horizontal and homogeneous sample
Rig set-up	Single planar and vertical basement fault
Kinematic	Dextral strike-slip
Basal interface	Metal baseplate with rubber sheet
Total displacement	7 cm
Average displacement rate	4.12 mm min^{-1}
Duration	17 min
DIC frame rate	1 Hz, $\Delta t = 1$ s
DIC raw data	*c.* 1000 images

for each displacement step shown in Figure 13 was, progressively, 0.93, 1.34, 1.35, 1.58, 1.62 and 1.68 cm, with a final damage zone width spanning, along strike, 0.75–1.68 cm, corresponding a fault damage zone width ranging over 8–17.89 m in nature.

6. Discussion

The sand–hemihydrate GRAM aggregate enables the simulation of multi-scale fault–fracture processes in scaled physical experiments. The material is suitable for forming cohesive aggregates capable of deforming by shear and tensile failure while preserving the nonlinear behaviour of granular materials. The dynamic scaling provided by GRAM material enables the simulation of fault damage zones at the structural scale, with 1 cm in the model corresponding to 10.65 m in nature.

The material was applied in a strike-slip experiment series to evaluate its applicability in scaled analogue experiments. The experiment GRAM test-7 described in Section 5.c above demonstrated the characteristic geometries, kinematics and dynamics of fracture nucleation and damage zone evolution leading to an interconnected shear zone, that is, a primary deformation zone (PDZ).

The observed geometries are representative of a strike-slip shear zone and can be directly compared with natural systems. The models developed with GRAM represent relatively low-strain fault systems, similar to the fault systems developed by earthquake surface ruptures. In Figure 14, we compare the GRAM test-7 model with an example of low-strain shear zone (*c.* 3.5 m displacement), dextral strike-slip earthquake event, the Greendale Fault, New Zealand (Quigley *et al.* 2010). In this case, we used this natural example to validate the models but did not specifically scale the experiment dynamically to the surficial alluvial sediments affected by the earthquake event shown in Figure 14. The structural features of the two shear zones show high similarity to the main structures represented by Riedel shears and the smaller conjugate shear fractures (R') as minor structures. In the model, the R shears developed at *c.* 22° clockwise with respect to the trace of the basement fault and formed an angle of *c.* 75° with the R' shears (Fig. 14b). In the natural system, the R shears formed at *c.* 26° from the plane of the imposed shear and are at *c.* 56° to the conjugate R' shears (Fig. 14d). The level of deformation is higher in the model with respect to the prototype, where the R shears are not directly linked and the Y shears are only incipient. As a result, in contrast to the model (Fig. 14a, b), the shear zone is not yet completely interconnected (Fig. 14c, d). P shears are not observed in the model and in the prototype, confirming, in both cases, the relatively low-strain level of the shear zones.

Overall, the experimental results demonstrated that the sand–hemihydrate GRAM can be applied in scaled experiments for the simulation of fault–fracture processes in fault damage zones observable at outcrop-scale resolution. Consequently, our GRAM experiments can be directly compared with natural fault systems.

6.a. Sand–hemihydrate challenges and limitations

As derived from systematic material testing, sand-hemihydrate aggregates fulfilled all the GRAM requirements for fault–fracture simulation (Section 4). The sand–hemihydrate aggregates were further examined in terms of physical and mechanical properties, with the sample preparation procedure including sample homogeneity and properties of diverse mixing ratios. We also evaluated the experiment set-up, deformation rig features, and experiment volume preparation and dimensions to outline potential improvements and limitations.

6.a.1. Physical and mechanical properties

As part of the sample preparation with consistent mechanical parameters, the impact of the residual water content on the material properties was analysed in detail. Uniaxial compression test results highlighted the clear influence of the drying duration on the mechanical properties of the material. The compressive strength showed a linear relationship with drying time (Fig. 15a).

Consequently, samples with different physical and mechanical characteristics are obtained with a longer/shorter drying time or with different ambient conditions. This aspect critically influences the reproducibility of GRAM properties in different experiments. To tackle this problem, during the drying stage the moisture content of the samples was analysed by time-series data of the sample weight at 24-hour intervals to monitor the water loss through time. The rate of water loss of the samples (at controlled laboratory ambient temperature conditions of 23 ± 4°C and 33 ± 6% humidity) stabilized within 5 days, with a decrease of the initial amount of water in weight by 80–90% (Fig. 15b).

The percentage of water loss seemed to be a more accurate parameter to determine the completion of the drying process, rather than defining a fixed time, since the process is strongly influenced by the environmental humidity and temperature conditions in the laboratory. The oven-drying procedure was precluded because the volume dimension (100 × 60 × 10 cm) hinders the transport of the sample from the oven and to the rig without risk of damage. Oven-drying was therefore not applied to smaller samples (i.e. for UCT and RST) since the condition was not replicable for the experiments samples. Consequently, we established that the sand–hemihydrate samples were defined ready, either for mechanical tests or analogue experiments, once the water loss reached 80–90%.

The material compaction applied during the sample preparation is important for the homogeneity of samples (Fig. 11a). Nevertheless, its impact on the density of GRAM experiment volumes should be further evaluated in future. The linear interpolation of mass/volume ratios (Fig. 10) suggests a slight increase in density by reducing the volume of the samples. This bias is the result of the difficulty of directly weighing the 100 × 60 × 10 cm

https://doi.org/10.1017/S0016756821001321 Published online by Cambridge University Press

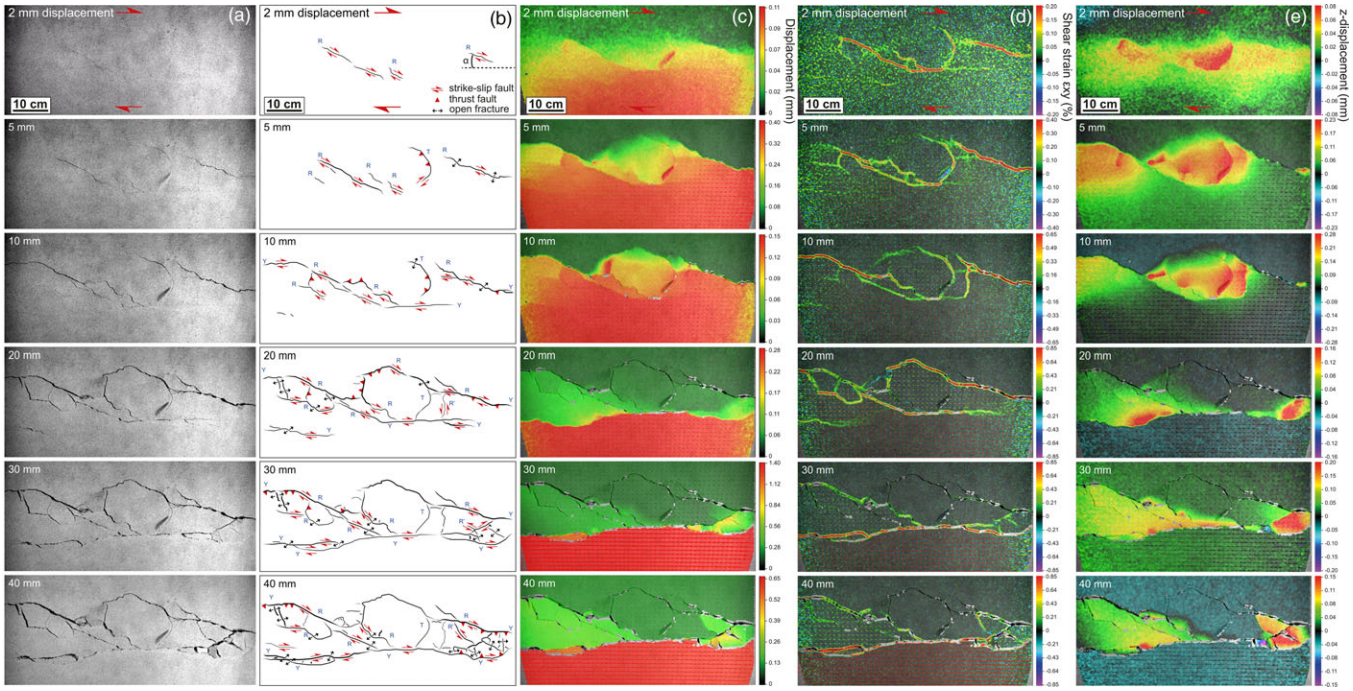

Fig. 13. DIC time-series images of sand–hemihydrate 2% sample surface during GRAM test-7 experiment: (a) image source data; (b) structural map; (c) displacement field (mm) with vector displacement; (d) shear strain ϵ_{xy} (%) with vectors displacement; and (e) *z*-displacement (mm) with vector displacement. R – Riedel shear; R' – R' shear; Y – Y shear; T – thrust fault.

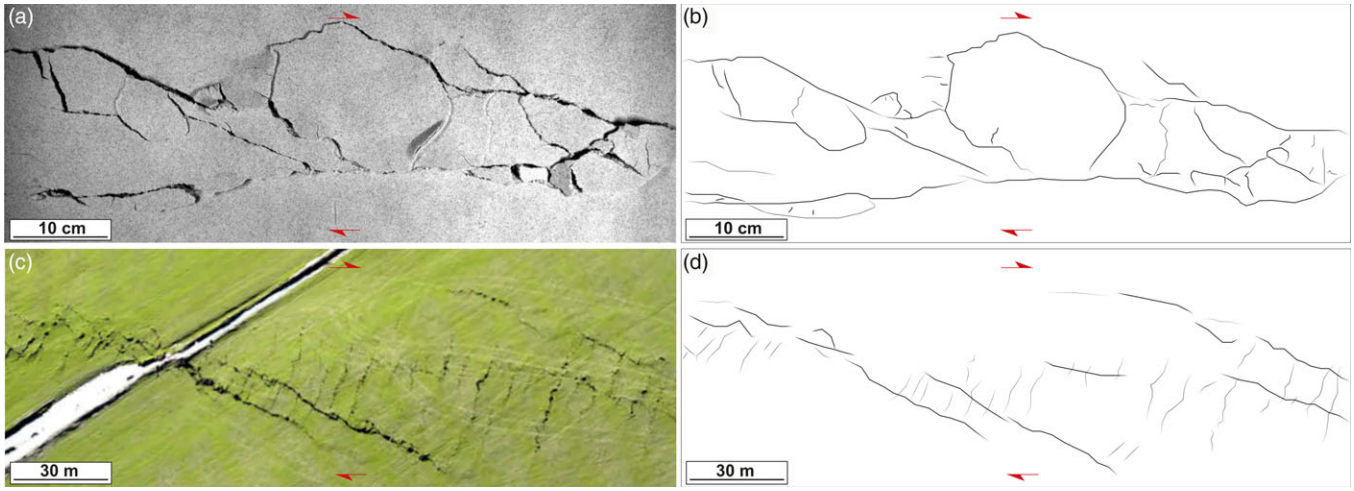

Fig. 14. Model comparison with natural strike-slip shear zone (Greendale Fault surface rupture, New Zealand; Quigley *et al.* 2010). (a) GRAM test-7 experiment surface with (b) structural map of the developed structures and (c) aerial photograph of the Greendale Fault surface rupture, New Zealand (aerial photograph from Quigley *et al.* 2010), with (d) structural map of the developed structures.

samples, for which the mass (g) was estimated from the sample preparation materials before mixing them, slightly underestimating it. Although the resulting overestimation of density was relatively minor (1.38 g cm^{-3} instead of 1.36 g cm^{-3}), the density used to calculate the dynamic scaling was obtained considering only the mechanical test samples (UCT, RST Cell 2 and RST Cell 1 + 2).

Furthermore, the effect of the ratio of the sand–hemihydrate mixture on mechanical properties was analysed by testing samples with a range of mixing ratios. Sand–hemihydrate aggregates with 1% to 4% of hemihydrate (on the total dry parts weight) were tested.

Uniaxial compression test results (Table 9) showed no significant variation of Young's modulus between the different mixing ratios, with average values ranging from 2.09 to 2.99 MPa. A linear trend was observed for the values of maximum normal load applied during the test (F_{max}) and the normal load registered at the first break of the sample (F_{break}). The compressive strength showed a linear relationship with the hemihydrate concentration (Fig. 15c).

https://doi.org/10.1017/S0016756821001321 Published online by Cambridge University Press

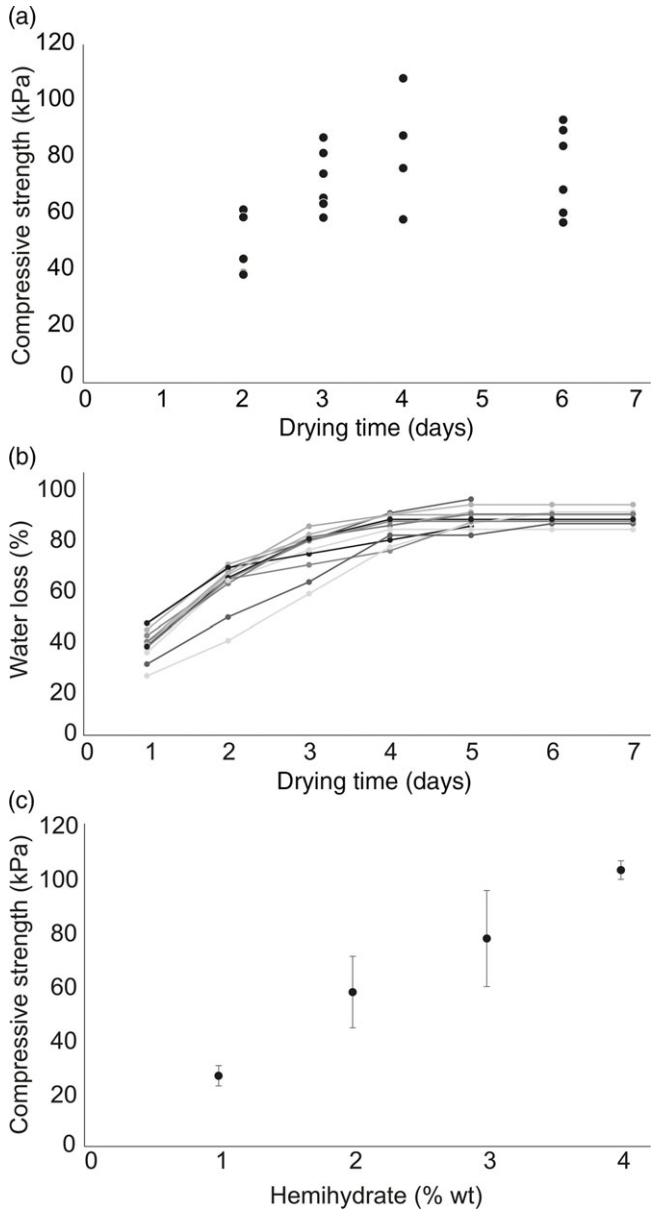

Fig. 15. (a) Compressive strength variation trend with different drying time; (b) percentage of water evaporation with respect to the initial amount in weight, monitored through time during the drying stage and (c) compressive strength values for different concentrations of hemihydrate in sand–hemihydrate aggregates, after uniaxial compression tests.

It is reasonable to assume that such a relationship is similarly observed for the material cohesive strength (Haug *et al.* 2014). This aspect should be further investigated in future studies. The observed linear relationships between the mixing ratio and GRAM strength enables the adjustment of GRAM mechanical properties and GRAM scaling for specific experiment applications and resolutions.

6.a.1.1. Dynamic scaling. The dynamic scaling of GRAM (Section 4.d) provides a geometric scaling factor L^* of 9.39×10^{-4} (1 cm in the model corresponding to 10.65 m in nature). The geometric scaling factor was calculated considering an arbitrary natural prototype with a cohesive strength of 15 MPa and 2.43 g cm^{-3} of density, corresponding to the limestone of the Lueders Fomation (see online Supplementary Table S1). To analyse the role of different lithologies on the model resolution, we calculated the dynamic scaling of GRAM with respect to a sandstone (Tennessee Formation), a marble and a granite (see online Supplementary Table S1). The resulting geometrical scaling factors (Table 10) showed that with the sandstone, the marble and the granite as a prototype rock the deduced model resolution would be appropriate for simulating fault damage zone processes observed at the outcrop scale (1 cm in the model corresponding to 36.40, 69.26 and 20.18 m, respectively; Fig. 16).

6.a.2. Experiment set-up

Beyond homogeneous material volumes, scaled analogue experiments can simulate geological heterogeneities in their set-up. In GRAM experiments, a mechanical layering representing a layered sequence can be introduced as part of the preparation of GRAM aggregates. The mechanical layer thickness has a critical impact on the fracture propagation and the spatial distribution of fracture spacing and aperture in strata-bound fracture sets. To ensure the sample homogeneity, either for RST, UCT or experiment samples, the samples were compacted only when all the material was added to the cell, cylinder or rig (Section 5.a). However, in the sample preparation tests, we prepared sand–hemihydrate UCT samples by varying the sample preparation procedure. Namely, we observed that by filling and compacting the samples in different steps we obtained mechanical inhomogeneities representing the bed surfaces. During the UCTs these layers acted as a mechanical layer with respect to fracture propagation (Fig. 17). Potentially, the experiment samples could be prepared following this workflow and characterizing the model with beds, therefore enabling the investigation of the interaction between mechanical layer thickness and fracture propagation processes in scaled experiments.

As discussed in Section 5.a, a strike-slip setting was chosen for the prototype experiments because the experiment surface deformation represents tectonic material transport in the σ_1–σ_3 principal plane of stress. However, the experiment series showed that some improvements can be applied in terms of rig set-up. First, the deformation was manually driven by a hydraulic winch pulling one of the two baseplates. This was reflected by the formation of asymmetric shear zones characterized by a moving and a static block during the simulation. Also, the deformation rate was not constant, but was affected by the perception of the operator. For the GRAM test experiments, stepper motors used for generic sandbox experiments could not be utilized due to the high strength of the model material. The electronic motors available in the analogue tectonic modelling laboratories of the Department of Earth Sciences at Royal Holloway, University of London (ATML@RHUL) are designed for experiments consisting of nearly cohesionless and low-strength materials, not applicable to the GRAM prototypes. The application of more powerful electric motors or attenuators to deform the cohesive sand–hemihydrate aggregates in the future will enable a constant and controlled deformation rate during the experiment.

The presented strike-slip experiment series demonstrated the suitability of GRAM to simulate the kinematic and dynamic processes of shear zone evolution, although, with the experiment set-up described, only a relatively low level of strain was achieved before the superimposition of several pop-up structures limited the observation of primary shear zone features. With increasing displacement, these uplifted domains obstructed the surrounding structures in the PDZ. As seen in the analysed experiment (Fig. 13), in the high-strain stages the DIC maps show local data

https://doi.org/10.1017/S0016756821001321 Published online by Cambridge University Press

Table 9. Uniaxial compression test results for sand–hemihydrate samples at different mixing ratios: 1%, 2%, 3% and 4%. The error is the standard deviation of the mean values after multiple measurements (a total of 53 samples were tested).

	1%	2%	3%	4%
E_{mod} (MPa)	2.12 ± 1.51	2.99 ± 1.74	2.09 ± 1.46	2.53 ± 1.15
F_{max} (N)	177 ± 15.71	291.23 ± 99.58	353.84 ± 267.17	405.75 ± 103.75
dL (mm)	1.5 ± 0.28	1.9 ± 0.48	1.96 ± 0.54	1.32 ± 0.19
F_{break} (N)	35.41 ± 3.15	61.08 ± 29.91	76.51 ± 52.85	81.13 ± 39.76
dL (mm)	1.98 ± 0.44	2.27 ± 0.51	2.36 ± 0.73	1.8 ± 0.28

Table 10. Dynamic scaling provided by GRAM with different natural prototypes (from online Supplementary Table S1, available at http://journals.cambridge.org/geo)

Natural prototype	ρ_m (g cm^{-3})	ρ_n (g cm^{-3})	C_m (kPa)	C_n (MPa)	L^*	Model resolution L_n (m)
Sandstone	1.36	2.37	7.88	50	2.75×10^{-4}	36.4
Marble	1.36	2.74	7.88	110	1.44×10^{-4}	69.26
Granite	1.36	2.65	7.88	31	4.95×10^{-4}	20.18

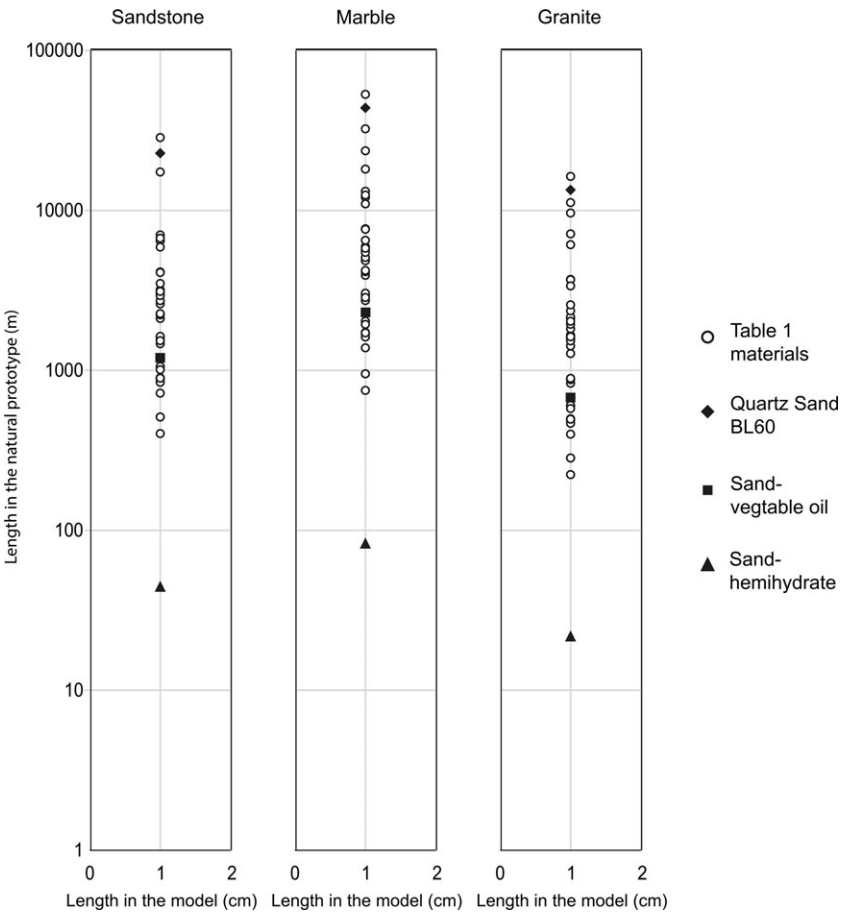

Fig. 16. Comparison chart of the model resolution, in terms of geometric scaling factor, provided by quartz sand BL60, sand–vegetable oil aggregates and the developed sand–hemihydrate GRAM. The dynamic scaling was calculated considering different prototypes, namely, sandstone, marble and granite (see online Supplementary Table S2).

gaps corresponding to the pop-up structures. As a result, the total finite displacement of the experiment set-up was limited to low-strain shear and damage zones.

The block uplift is caused by complex fault geometries characteristic of strike-slip tectonics. Different set-ups simulating dip–slip faults may enable an ideal damage zone simulation with continuous high-resolution DIC monitoring since the experiment hanging-wall would provide the confining pressure.

In analogue modelling studies involving granular model materials, after completion of the experiments the models are commonly saturated with a gelatine–water solution and, once dried, cross-sectional sequential slices are provided. This procedure

https://doi.org/10.1017/S0016756821001321 Published online by Cambridge University Press

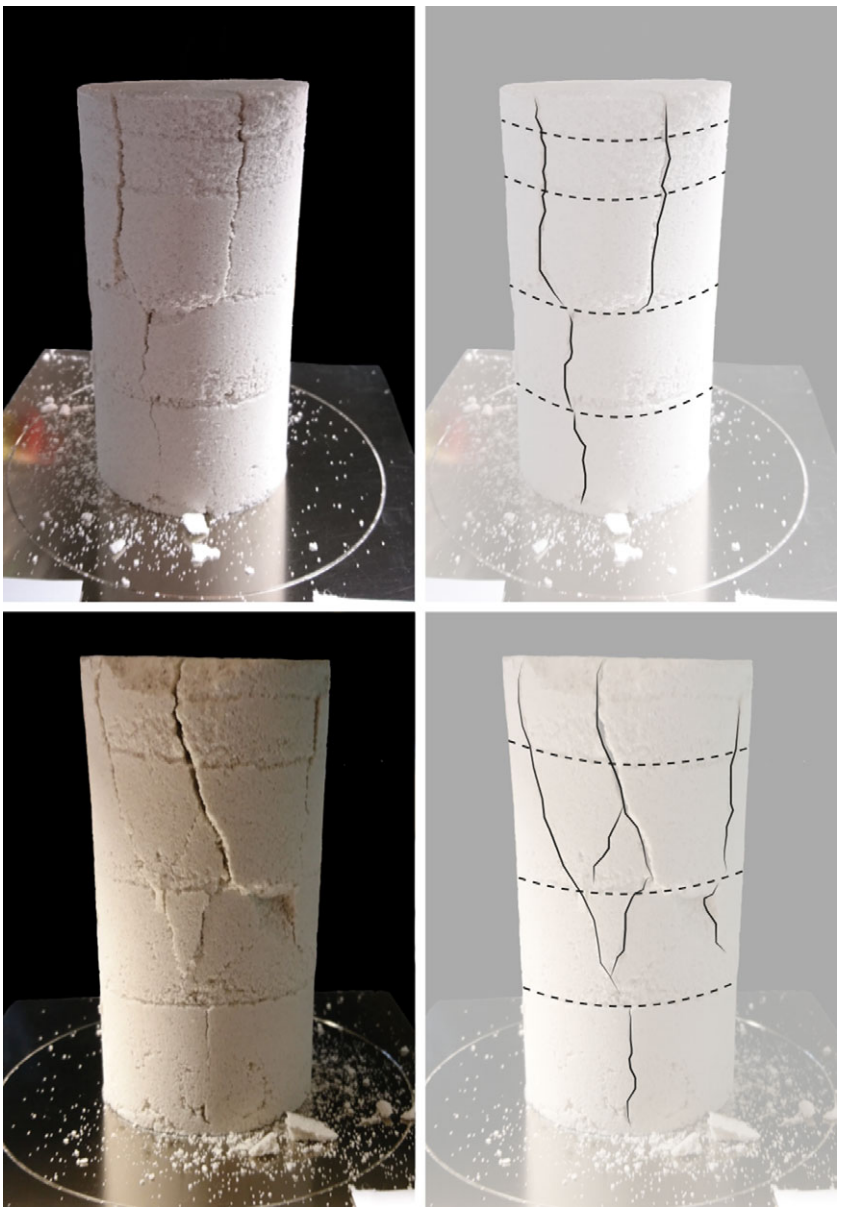

Fig. 17. UCT samples prepared by generating different mechanical layers, and schematic representations of the fracture–mechanical layer interaction.

allows the analysis of the final structures in 3D volumes. Early slicing tests were conducted on GRAM experiments by filling the open fractures generated during the experiment with dry granular sands then saturating the model with a diluted gelatine solution. However, this procedure will need major tests and further refinement to determine whether the different materials and the moisture conditions of the samples and the gelatine solution can be used to optimize slicing procedures.

7. Conclusions and outlook

We have developed a new granular rock-analogue material (GRAM), aimed at enabling the simulation of coupled fault–fracture processes at structural scales. Four aggregates were evaluated as potential GRAM candidates, based on quartz sand in a mixture with a cementing agent, and were tested for their physical and mechanical suitability. The GRAM needed to form cohesive and mechanically homogeneous aggregates, deforming by shear and tensile failure, while preserving the nonlinear behaviour of dry granular sands and providing a specific dynamic scaling. The latter was established so that the geometric scaling factor ensured a model resolution within the outcrop scale, that is, 1 cm in the model corresponding to 1–100 m in the prototype.

The material development tests demonstrated that sand–hemihydrate aggregates satisfied all the GRAM material requirements. The material showed a density of 1.36 g cm^{-3} and cohesion of 7.88 kPa, providing a geometric scaling factor (calculated for a prototype rock with 15 MPa cohesive strength and 2.43 g cm^{-3} density) suitable for the required model resolution, with 1 cm in the model corresponding to 10.65 m in nature. The mechanical properties of the GRAM material could be adjusted by changing the mixing ratios, with an observed linear relationship between the cementing agent percentage (hemihydrate) and the material strength.

As a larger-scale test, the material was prepared in larger volumes for strike-slip scaled analogue experiments. The experiment series, analysed by means of digital image correlation (DIC) techniques, showed the kinematic and dynamic evolution of a

https://doi.org/10.1017/S0016756821001321 Published online by Cambridge University Press

strike-slip shear zone from the early stages of fracture nucleation to the interconnected architecture of the final primary deformation zone and related fault damage zone. The final model was directly compared with a natural earthquake rupture, highlighting the similar architecture of the two shear zones and validating the model itself.

The developed GRAM material will enable the simulation of fault and fracture processes at a high resolution and representative structural scale, allowing the investigation of fault damage zone evolution. The mechanical properties of GRAM can also be modified by varying the mixing ratios, enabling the adjustment of the model dynamic scaling for the simulation of different tectonic processes with specific experimental resolution.

Supplementary material. For supplementary material accompanying this paper visit https://doi.org/10.1017/S0016756821001321

Acknowledgements. The research described in this paper includes work conducted during a PhD study undertaken as part of the Natural Environment Research Council (NERC) Centre for Doctoral Training (CDT) in Oil & Gas (grant no. NE/M00578X/1) sponsored by the Royal Holloway University of London, whose support is gratefully acknowledged. We extend our thanks to Kevin D'Souza for the photographs and the technical help and to Jerry Morris for the engineering support at RHUL Analogue Tectonic Modelling Laboratories. We acknowledge the guest editor Fabrizio Balsamo, Yago Nestola and an anonymous reviewer for their helpful remarks and suggestions for revision.

Declaration of interest. The authors declare that the research was conducted in the absence of any commercial or financial relationships that could imply a potential conflict of interest.

References

Abdelmalak MM, Bulois C, Mourgues R, Galland O, Legland JB and Gruber C (2016) Description of new dry granular materials of variable cohesion and friction coefficient: implications for laboratory modeling of the brittle crust. *Tectonophysics* **684**, 39–51.

Adam J, Klinkmüller M, Schreurrs G and Wieneke B (2013a) 4D Simulation of shear localization and strain history in fault systems: insights from physical experiments, X-ray computed tomography and tomographic digital image correlation. *Journal of Structural Geology* **55**, 127–49.

Adam J, Klinkmüller M, Schreurs G and Wieneke B (2013b) Quantitative 3D strain analysis in analogue experiments simulating tectonic deformation: integration of X-ray computed tomography and digital volume correlation techniques. *Journal of Structural Geology* **55**, 127–49.

Adam J, Lohrmann J, Hoth S, Kukowski N and Oncken O (2002) Strain variation and partitioning in thrust wedges: High-resolution data from scaled sandbox experiments by 2D-3D PIV analysis. *Bollettino di Geofisica Teorica ed Applicata* **42**, 123–6.

Adam J, Schreurs G, Klinkmüller M and Wieneke B (2008) 2D/3D Strain localisation and fault simulation in analogue experiments: insights from X-ray computed tomography and tomographic image correlation. *Bollettino di Geofisica Teorica ed Applicata* **49**, 21–22.

Adam J, Urai JL, Wieneke B, Oncken O, Pfeiffer K, Kukowski N, Lohrmann J, Hoth S, van der Zee W and Schmatz J (2005) Shear localisation and strain distribution during tectonic faulting—new insights from granular-flow experiments and high-resolution optical image correlation techniques. *Journal of Structural Geology* **27**, 283–301.

Anderson EM (1951) *The Dynamics of Faulting and Dyke Formation with Applications to Britain*. New York: Hafner Publishing Company.

Aydin A (2000) Fractures, faults, and hydrocarbon entrapment, migration and flow. *Marine and Petroleum Geology* **17**, 797–814.

Basu A, Mishra DA and Roychowdhury K (2013) Rock failure modes under uniaxial compression, Brazilian, and point load tests. *Bulletin of Engineering Geology and the Environment* **72**, 457–75.

Billi A, Salvini F and Storti F (2003) The damage zone-fault core transition in carbonate rocks: implications for fault growth, structure and permeability. *Journal of Structural Geology* **25**, 1779–94.

Bitri A, Brun JP, Chantraine J, Guennoc P, Marquis G, Marthelot JM, Perrin J, Pivot F and Truffert C (1997) Structure crustale du bloc cadomien de Bretagne Nord (France); sismique reflexion verticale et sondage magnetotellurique (projet Geofrance 3D – Armor). [Crustal structure of the Cadomian Block in northern Brittany, France; vertical seismic reflection and magnetotelluric sounding, part of the Geofrance 3D Armor Project.] Comptes Rendus de l'Academie des Sciences, Serie II. *Sciences de la Terre et des Planetes* **325**, 171–7.

Bonanno E, Bonini L, Basili R, Toscani G and Seno S (2017) How do horizontal, frictional discontinuities affect reverse fault-propagation folding? *Journal of Structural Geology* **102**, 147–67.

Bonini L, Basili R, Toscani G, Burrato P, Seno S and Valensise G (2016) The effects of pre-existing discontinuities on the surface expression of normal faults: Insights from wet-clay analog modeling. *Tectonophysics* **684**, 157–75.

Bonini L, Sokoutis D, Mulugeta G and Katrivanos E (2000) Modelling hanging wall accommodation above rigid thrust ramps. *Journal of Structural Geology* **22**(8), 1165–79.

Brizzi S, Funiciello F, Corbi F, Di Giuseppe E and Mojoli G (2016) Salt matters: how salt affects the rheological and physical properties of gelatine for analogue modelling. *Tectonophysics* **679**, 88–101.

Byerlee J (1978) Friction of rocks. *Pure and Applied Geophysics* **116**, 615–26.

Caine JS, Evans JP and Forster CB (1996) Fault zone architecture and permeability structure. *Geology* **24**, 1025–8.

Chemenda AI, Nguyen SH, Petit JP and Ambre J (2011) Experimental evidences of transition from mode I cracking to dilatancy banding. *Comptes Rendus Mécanique* **339**, 219–25.

Chester FM and Logan JM (1987) Composite planar fabric of gouge from the Punchbowl fault, California. *Journal of Structural Geology* **9**, 621–34.

Childs C, Nicol A, Walsh JJ and Watterson J (1996) Growth of vertically segmented normal faults. *Journal of Structural Geology* **18**, 1389–97.

Choi JH, Edwards P, Ko K and Kim YS (2016) Definition and classification of fault damage zones: A review and a new methodological approach. *Earth-Science Reviews* **152**, 70–87.

Choi JH, Jin K, Enkhbayar D, Davvasambuu B, Bayasgalan A and Kim YS (2012) Rupture propagation inferred from damage patterns, slip distribution, and segmentation of the 1957 MW8.1 Gobi-Altay earthquake rupture along the Bogd fault, Mongolia. *Journal of Geophysical Research: Solid Earth* **117**, B12401.

Cloos H (1928) Experimente zur inneren Tektonik. Centralblatt für Mineralogie, Geologie und Paläontologie 5, 609–21.

Cobbold P, Durand S and Mourgues R (2001) Sandbox modelling of thrust wedges with fluid-assisted detachments. *Tectonophysics* **334**, 245–58.

Corbi F, Funiciello F, Moroni M, Van Dinther Y, Mai PM, Dalguer LA and Faccenna C (2013) The seismic cycle at subduction thrusts: 1. Insights from laboratory models. *Journal of Geophysical Research: Solid Earth* **118**, 1483–501.

Costa E and Vendeville BC (2002) Experimental insights on the geometry and kinematics of fold-and-thrust belts above weak, viscous evaporitic decollement. *Journal of Structural Geology* **24**, 1729–39.

Cowie PA and Shipton ZK (1998) Fault tip displacement gradients and process zone dimensions. *Journal of Structural Geology* **20**, 983–97.

Crider JG and Peacock DCP (2004) Initiation of brittle faults in the upper crust: a review of field observations. *Journal of Structural Geology* **26**, 691–707.

Cruz L, Malinski J, Wilson A, Take WA and Hilley G (2010) Erosional control of the kinematics and geometry of fold-and-thrust belts imaged in a physical and numerical sandbox. *Journal of Geophysical Research: Solid Earth* **115**, 1–15.

Cruz L, Teyssier C, Perg L, Take A and Fayon A (2008) Deformation, exhumation, and topography of experimental doubly-vergent orogenic wedges subjected to asymmetric erosion. *Journal of Structural Geology* **30**, 98–115.

Davis D and Dahlen JSFA (1983) Mechanics of fold-and-thrust belts and accretionary wedges. *Journal of Geophysical Research* **88**, 1153–72.

Davis GH (1984) *Structural Geology of Rocks and Regions*. New York: Wiley.

Dooley TP and Schreurs G (2012) Analogue modelling of intraplate strike-slip tectonics: a review and new experimental results. *Tectonophysics* **574–575**, 1–71.

Dotare T, Yamada Y, Adam J, Hori T and Sakaguchi H (2016) Initiation of a thrust fault revealed by analog experiments. *Tectonophysics* **684**, 148–56.

Faulkner DR, Jackson CAL, Lunn RJ, Schlische RW, Shipton ZK, Wibberley CAJ and Withjack MO (2010) A review of recent developments concerning the structure, mechanics and fluid flow properties of fault zones. *Journal of Structural Geology* **32**, 1557–75.

Ferrill DA, Morris AP, McGinnis RN, Smart KJ and Ward WC (2011) Fault zone deformation and displacement partitioning in mechanically layered carbonates: the Hidden Valley fault, central Texas. *AAPG Bulletin* **95**, 1383–97.

Fossen H (2020) Fault classification, fault growth and displacement. In *Regional Geology and Tectonics: Principles of Geologic Analysis* (eds N Scarselli, J Adam, D Chiarella, DG Roberts and AW Bally), pp. 119–47. Amsterdam: Elsevier.

Galland O, Cobbold PR, Hallot E, de Bremond d'Ars J and Delavaud G (2006) Use of vegetable oil and silica powder for scale modelling of magmatic intrusion in a deforming brittle crust. *Earth and Planetary Science Letters* **243**, 786–804.

Gomes CJS (2013) Investigating new materials in the context of analog-physical models. *Journal of Structural Geology* **46**, 158–66.

Gudmundsson A, De Guidi G and Scudero S (2013) Length–displacement scaling and fault growth. *Tectonophysics* **608**, 1298–309.

Gudmundsson A, Simmenes TH, Larsen B and Philipp SL (2010) Effects of internal structure and local stresses on fracture propagation, deflection, and arrest in fault zones. *Journal of Structural Geology* **32**, 1643–55.

Gutscher MA, Kukowski N, Malavieille J and Lallemand S (1996) Cyclical behavior of thrust wedges; insights from high basal friction sandbox experiments. *Geology* **24**, 135–8.

Gutscher MA, Kukowski N, Malavieille J and Lallemand S (1998) Material transfer in accretionary wedges from analysis of a systematic series of analog experiments. *Journal of Structural Geology* **20**, 407–16.

Handin J (1966) Handbook of physical constants. *Geological Society of America Memoirs* **97**, 223–90.

Hatem AE, Cooke ML and Toeneboehn K (2017) Strain localization and evolving kinematic efficiency of initiating strike-slip faults within wet kaolin experiments. *Journal of Structural Geology* **101**, 96–108.

Haug ØT, Rosenau M, Leever K and Oncken O (2014) *Modelling Fragmentation in Rock Avalanches*. Cham: Springer International Publishing, pp. 93–100.

Healy D, Jones RR and Holdsworth RE (2006) Three-dimensional brittle shear fracturing by tensile crack interaction. *Nature* **439**, 64–7.

Henza AA, Withjack MO and Schlische RW (2010) Normal-fault development during two phases of non-coaxial extension: an experimental study. *Journal of Structural Geology* **32**, 1656–67.

Hoek E and Bieniawski ZT (1965) Brittle fracture propagation in rock under compression. *International Journal Fracture Mechanics* **1**, 137–55.

Hoek E and Brown ET (1988) The Hoek-Brown failure criterion – a 1988 update. In *Rock Engineering for Underground Excavations* (ed. JC Curran), 31–38. Proceedings of 15th Canadian Rock Mechanics Symposium. Toronto: University of Toronto.

Hoek E and Martin CD (2014) Fracture initiation and propagation in intact rock – a review. *Journal of Rock Mechanics and Geotechnical Engineering* **6**, 287–300.

Holland M, Urai JL and Martel S (2006) The internal structure of fault zones in basaltic sequences. *Earth and Planetary Science Letters* **248**, 286–300.

Hoth S, Adam J, Kukowski N and Oncken O (2006) Influence of erosion on the kinematics of divergent orogens: Results from scaled sandbox simulations. *Geological Society of America Special Paper* **398**, 201–25.

Hoth S, Hoffmann-Rothe A and Kukowski N (2007) Frontal accretion: an internal clock for bivergent wedge deformation and surface uplift. *Journal of Geophysical Research: Solid Earth* **112**, 1–17.

Hoth S, Kukowski N and Oncken O (2008) Distant effects in bivergent orogenic belts – how retro-wedge erosion triggers resource formation in proforeland basins. *Earth and Planetary Science Letters* **273**, 28–37.

Hubbert MK (1937) *Theory of Scale Models as Applied to the Study of Geologic Structures*. Chicago: University of Chicago.

Huiqui L, McClay KR and Powell D (1992) Physical models of thrust wedges. In *Thrust Tectonics* (ed KR McClay), pp. 71–81. London: Chapman & Hall.

Jaeger JC and Cook NGW (1969) *Fundamentals of Rock Mechanics*. London: Methuen.

Kim YS, Peacock DCP and Sanderson DJ (2003) Mesoscale strike-slip faults and damage zones at Marsalforn, Gozo Island, Malta. *Journal of Structural Geology* **25**, 793–812.

Kim YS, Peacock DCP and Sanderson DJ (2004) Fault damage zones. *Journal of Structural Geology* **26**, 503–17.

Kim YS and Sanderson DJ (2009) Earthquake and fault propagation, displacement and damage zones. In *Structural Geology: New Research* (eds SJ Landowne and GM Hammler). New York: Nova Science.

Klinkmüller M, Schreurs G, Rosenau M and Kemnitz H (2016) Properties of granular analogue model materials: a community wide survey. *Tectonophysics* **684**, 23–38.

Koyi HA (1997) Analogue modelling; from a qualitative to a quantitative technique; a historical outline. *Journal of Petroleum Geology* **20**, 223–38.

Krantz RW (1991) Measurements of friction coefficients and cohesion for faulting and fault reactivation in laboratory models using sand and sand mixtures. *Tectonophysics* **188**, 203–7.

Krézsek C, Adam J and Grujic D (2007) Mechanics of fault and expulsion rollover systems developed on passive margins detached on salt: insights from analogue modelling and optical strain monitoring. In *Structurally Complex Reservoirs* (eds SJ Jolley, D Barr, JJ Walsh and RJ Knipe), pp. 103–21. Geological Society of London, Special Publication no. **292**.

Kukowski N, Lallemand SE, Malavieille J, Gutscher MA and Reston TJ (2002) Mechanical decoupling and basal duplex formation observed in sandbox experiments with application to the Western Mediterranean Ridge accretionary complex. *Marine Geology* **3068**, 1–13.

Lallemand SE, Lewis KB and Collot JY (1994) Sandbox modelling of seamount subduction and possible applications in New Zealand. In *Geological Society of New Zealand 1994 Annual Conference; Programme and Abstracts* (eds H Neil, JL Gillespie, V Moon and R Briggs), p. 109. Christchurch: Geological Society of New Zealand.

Lohrmann J, Kukowski N, Adam J and Oncken O (2003) The impact of analogue material properties on the geometry, kinematics, and dynamics of convergent sand wedges. *Journal of Structural Geology* **25**, 1691–711.

Maestrelli D, Bonini M, Corti G, Del Ventisette C, Moratti G and Montanari D (2021) A database of laboratory analogue models of caldera collapse testing the role of inherited structures. *Frontiers in Earth Science* **9**, 1–27.

Mandl G (1988) *Mechanics of Tectonic Faulting: Models and Basic Concepts*. New York: Elsevier.

Marcher T and Vermeer PA (2001) Macromodelling of softening in non-cohesive soils. In *Continuous and Discontinuous Modelling of Cohesive-Frictional Materials* (eds PA Vermeer, HJ Herrmann, S Luding, W Ehlers, S Diebels and E Ramm), pp. 89–110. Berlin, Heidelberg: Springer.

Marone C (1998) The effect of loading rate on static friction and the rate of fault healing during the earthquake cycle. *Nature (London)* **391**, 69–72.

Marrett R and Allmendinger RW (1992) Amount of extension on "small" faults: an example from the Viking graben. *Geology* **20**, 47–50.

McClay KR (1996) Recent advances in analogue modelling: uses in section interpretation and validation. In *Modern Developments in Structural Interpretation, Validation and Modelling* (eds PG Buchanan and DA Nieuwland), pp. 201–25. Geological Society of London, Special Publication no. 99.

McClay KR, Dooley T and Lewis G (1998) Analog modeling of progradational delta systems. *Geology* **26**, 771–4.

McClay KR and Ellis PG (1987a) Analogue models of extensional fault geometries. In *Continental Extensional Tectonics* (eds MP Coward, JF Dewey and PL Hancock), pp. 109–25. Geological Society of London, Special Publication no. 28.

McClay KR and Ellis PG (1987b) Geometries of extensional fault systems developed in model experiments. *Geology* **15**, 341–4.

Micarelli L, Benedicto A and Wibberley CAJ (2006) Structural evolution and permeability of normal fault zones in highly porous carbonate rocks. *Journal of Structural Geology* **28**, 1214–27.

Moore DE and Lockner DA (1995) The role of microcracking in shear-fracture propagation in granite. *Journal of Structural Geology* **17**, 95–114.

Mouslopoulou V, Walsh JJ and Nicol A (2009) Fault displacement rates on a range of timescales. *Earth and Planetary Science Letters* **278**, 186–97.

Panien M, Schreurs G and Pfiffner A (2006) Mechanical behaviour of granular materials used in analogue modelling: insights from grain characterisation, ring-shear tests and analogue experiments. *Journal of Structural Geology* **28**, 1710–24.

Paterson MS (1978) *Experimental Rock Deformation*. New York: Springer.

Peacock DCP (2002) Propagation, interaction and linkage in normal fault systems. *Earth-Science Reviews* **58**, 121–42.

Peacock DCP and Sanderson DJ (1995) Strike-slip relay ramps. *Journal of Structural Geology* **17**, 1351–60.

Pons A and Mourgues R (2012) Deformation and stability of over-pressured wedges: insight from sandbox models. *Journal of Geophysical Research: Solid Earth* **117**, article B09404.

Poppe S, Holohan EP, Rudolf M, Rosenau M, Galland O, Delcamp A and Kervyn M (2021) Mechanical properties of quartz sand and gypsum powder (plaster) mixtures: implications for laboratory model analogues for the Earth's upper crust. *Tectonophysics* 814, 228976.

Quigley M, Dissen RV, Villamor P, Litchfield N, Barrell D, Furlong K, Stahl T, Duffy B, Bilderback E, Noble D, Townsend D, Begg J, Jongens R, Ries W, Claridge J, Klahn A, Mackenzie H, Smith A, Hornblow S, Nicol R, Cox S, Langridge R and Pedley K (2010) Surface rupture of the Greendale Fault during the Darfield (Canterbury) earthquake, New Zealand. *Bulletin of the New Zealand Society for Earthquake Engineering* **43**, 236–42.

Ramberg H (1981) *Gravity, Deformation and the Earth's Crust*. New York: Academic Press.

Ranalli G (2001) Experimental tectonics: from Sir James Hall to the present. *Journal of Geodynamics* **32**, 12.

Reber JE, Cooke ML and Dooley TP (2020) What model material to use? A Review on rock analogs for structural geology and tectonics. *Earth-Science Reviews* **202**, 1–21.

Reches Z and Lockner DA (1994) Nucleation and growth of faults in brittle rocks. *Journal of Geophysical Research: Solid Earth* **99**, 18159–73.

Riedel W (1929) Zur Mechanik geologischer Bruchstrukturen. *Zentral-blatt fur Mineralogie, Geologie und Paleontologie* 8, 354–68.

Rosenau M, Corbi F and Dominguez S (2017) Analogue earthquakes and seismic cycles: experimental modelling across timescales. *Solid Earth* **8**, 597–635.

Rosenau M, Lohrmann J and Oncken O (2009) Shocks in a box: An analogue model of subduction earthquake cycles with application to seismotectonic forearc evolution. *Journal of Geophysical Research: Solid Earth* **114**, 1–20.

Rosenau M and Oncken O (2009) Fore-arc deformation controls frequency-size distribution of megathrust earthquakes in subduction zones. *Journal of Geophysical Research: Solid Earth* **114**, 1–12.

Rossi D and Storti F (2003) New artificial granular materials for analogue laboratory experiments: aluminium and siliceous microspheres. *Journal of Structural Geology* **25**, 1893–99.

Santolaria P, Ferrer O, Rowan MG, Snidero M, Carrera N, Granado P, Muñoz JA, Roca E, Schneider CL, Piña A and Zamora G (2021) Influence of preexisting salt diapirs during thrust wedge evolution and secondary welding: Insights from analog modeling. *Journal of Structural Geology* **149**, 104374.

Schellart WP (2000) Shear test results for cohesion and friction coefficients for different granular materials; scaling implications for their usage in analogue modelling. *Tectonophysics* **324**, 1–16.

Scholz CH (2002) *The Mechanics of Earthquakes and Faulting*. Cambridge: Cambridge University Press.

Scholz CH and Cowie PA (1990) Determination of total strain from faulting using slip measurements. *Nature* **346**(6287), 837–39.

Schreurs G (1994) Experiments on strike-slip faulting and block rotation. *Geology* **22**, 567–70.

Schreurs G, Buiter SJH, Boutelier J, Burberry C, Callot JP, Cavozzi C, Cerca M, Chen JH, Cristallini E, Cruden AR, Cruz L, Daniel JM, Da Poian G, Garcia VH, Gomes CJS, Grall C, Guillot Y, Guzmán C, Hidayah TN, Hilley G, Klinkmüller M, Koyi HA, Lu CY, Maillot B, Meriaux C, Nilfouroushan F, Pan CC, Pillot D, Portillo R, Rosenau M, Schellart WP, Schlische RW, Take A, Vendeville B, Vergnaud M, Vettori M, Wang SH, Withjack MO, Yagupsky D and Yamada Y (2016) Benchmarking analogue models of brittle thrust wedges. *Journal of Structural Geology* **92**, 116–39.

Schreurs G, Buiter S, Boutelier D, Corti G, Costa E, Cruden A, Daniel JM, Hoth S, Koyi H, Kukowski N, Lohrman J, Ravaglia A, Schlische RW, Withjack MO, Yamada Y, Cavozzi C, Delventisette C, Brady JAE, Hoffman-Rothe A, Mengus JM, Montanari D and Nilforoushan F (2006) Analogue benchmarks of shortening and extension experiments. In *Analogue and Numerical Modelling of Crustal Scale Processes* (eds S Buiter and G Schreurs), pp. 1–27. Geological Society of London, Special Publication no. 253.

Schulze D (1994) A new ring shear tester for flowability and time consolidation measurements. In *Proceedings of International Particle Technology Forum*, Denver, Colorado, USA, pp. 11–16. New York: American Institute of Chemical Engineers.

Shipton ZK and Cowie PA (2003) A conceptual model for the origin of fault damage zone structures in high-porosity sandstone. *Journal of Structural Geology* **25**, 333–44.

Shipton ZK, Evans JP, Kirschner D, Kolesar PT, Williams AP and Heath J (2004) Analysis of CO2 leakage through 'low-permeability' faults from natural reservoirs in the Colorado Plateau, east-central Utah. In *Geological Storage of Carbon Dioxide* (eds SJ Baines and RH Worden), pp. 43–58. Geological Society, London, Special Publication no. 233.

Sibson RH (1989) Earthquake faulting as a structural process. *Journal of Structural Geology* **11**, 1–14.

Simpson GDH, Gueguen Y and Schneider F (2003) Analytical model for permeability evolution in microcracking rock. *Pure and Applied Geophysics* **160**, 999–1008.

Twiss RJ and Moores EM (1992) *Structural Geology*. San Francisco: WH Freeman & Co.

van Dinther Y, Gerya TV, Dalguer LA, Corbi F, Funiciello F and Mai PM (2013) The seismic cycle at subduction thrusts: 2. Dynamic implications of geodynamic simulations validated with laboratory models. *Journal of Geophysical Research: Solid Earth* **118**, 1502–25.

van Gent HW, Holland M, Urai JL and Loosveld R (2010) Evolution of fault zones in carbonates with mechanical stratigraphy – insights from scale models using layered cohesive powder. *Journal of Structural Geology* **32**, 1375–91.

Vermilye JM and Scholz CH (1998) The process zone: a microstructural view of fault growth. *Journal of Geophysical Research: Solid Earth* **103**, 12223–37.

Viggiani G and Hall SA (2008) Full-field measurements, a new tool for laboratory experimental geomechanics. In *4th Symposium on Deformation Characteristics of Geomaterials* (ed SE Burns, PW Mayne and JC Santamarina), pp. 3–26. Amsterdam: IOS Press.

von Hagke C, Kettermann M, Bitsch N, Bücken D, Weismüller C and Urai JL (2019) The effect of obliquity of slip in normal faults on distribution of open fractures. *Frontiers in Earth Science* **7**(18), 1–19.

Walsh JJ, Watterson J, Bailey WR and Childs C (1999) Fault relays, bends and branch-lines. *Journal of Structural Geology* **21**, 1019–26.

Wang WH and Davis D (1996) Sandbox model simulation of forearc evolution and noncritical wedges. *Journal of Geophysical Research* **101**, 329–11, 339.

White DJ, Take WA and Bolton MD (2001) Measuring soil deformation in geotechnical models using digital images and PIV analysis. In *10th International Conference on Computer Methods and Advances in Geomechanics,* Tucson, Arizona. Rotterdam: Balkema.

White DJ, Take WA and Bolton MD (2003) Soil deformation measurement using particle image velocimetry (PIV) and photogrammetry. *Géotechnique* **53**, 619–31.

Wibberley CAJ and Shipton ZK (2010) Fault zones: a complex issue. *Journal of Structural Geology* **32**, 1554–6.

Wibberley CAJ, Yielding G and Di Toro G (2008) Recent advances in the understanding of fault zone internal structure: a review. In *The Internal Structure of Flow Faults: Implications for Mechanical and Fluid-Flow Properties* (eds CAJ Wibberley, W Kurz, J Imber, RE Holdsworth,

https://doi.org/10.1017/S0016756821001321 Published online by Cambridge University Press

C Collettini), pp. 5–33. Geological Society of London, Special Publication no. 299.

Wolf H, König D and Triantafyllidis T (2003) Experimental investigation of shear band patterns in granular material. *Journal of Structural Geology* **25**, 1229–40.

Wu JE, McClay K and Frankowicz E (2015) Niger Delta gravity-driven deformation above the relict Chain and Charcot oceanic fracture zones, Gulf of Guinea: insights from analogue models. *Marine and Petroleum Geology* **65**, 43–62.

Yamada Y, Baba K, Miyakawa A and Matsuoka T (2014) Granular experiments of thrust wedges: Insights relevant to methane hydrate exploration at the Nankai accretionary prism. *Marine and Petroleum Geology* **51**, 34–48.

Zwaan F, Schreurs G and Adam J (2017) Effects of sedimentation on rift segment evolution and rift interaction in orthogonal and oblique extensional settings: Insights from analogue models analysed with 4D X-ray computed tomography and digital volume correlation techniques. *Global and Planetary Change* 171, 110–33.

https://doi.org/10.1017/S0016756821001321 Published online by Cambridge University Press